Multiscale flow alignment in cellulose nanocrystals controlled by surface topology

Journal of Colloid and Interface Science 723 (2026) 140913

Contents lists available at ScienceDirect

Journal of Colloid And Interface Science

journal homepage: www.elsevier.com/locate/jcis

Regular Article

Multiscale flow alignment in cellulose nanocrystals controlled by surface topology

Ases Akas Mishra[a,1], Amit Kumar Sonker[b,c,d,1], Kesavan Sekar[a,d,2], Marko Bek[a,d,e,f,2], Ann E. Terry[e,f], Kim Nygård[e,f], Stuart Ansell[e,f], Gunnar Westman[c,d,*], Roland Kádár[a,d,e,f,*]

[a] Department of Mechanical Engineering, Chalmers University of Technology, Göteborg, SE-41296, Sweden
[b] Cellulose Films and Coatings, Biomaterial Processing and Products, VTT, Technical Research Centre of Finland, Espo, 02150, Finland
[c] Department of Chemistry and Chemical Engineering, Chalmers University of Technology, Göteborg, SE-41296, Sweden
[d] Wallenberg Wood Science Centre (WWSC), Chalmers University of Technology, Göteborg, SE-41296, Sweden
[e] MAX IV Laboratory, Lund University, Lund, SE-22484, Sweden
[f] LINXS Institute for Advanced Neutron and X-ray Science, Lund University, Lund, SE-22484, Sweden

ARTICLE INFO

Keywords:
Cellulose nanocrystals
Rheology
Azedidinium salts
Surface linkers
Polarized light imaging
Small-angle x-ray scattering

ABSTRACT

We address how surface topology controls the multiscale flow alignment of cellulose nanocrystal (CNC) suspensions using a single in-situ experiment that combines rheology, polarized light imaging (PLI), and small-angle X-ray scattering (SAXS). Across a series of azetidinium-based dialkyl linker topologies, we resolve the propagation of alignment from the mesoscale (PLI) to the nanoscale (SAXS). While pristine CNC suspensions exhibit nearly-simultaneous onset of mesoscale birefringence and nanoscale alignment, surface-modified systems show a pronounced decoupling between these processes. In particular, the appearance of the Maltese-cross pattern in PLI systematically precedes detectable nanoscale alignment in SAXS. This is strongly dependent on linker topology. Extending the analysis beyond the Hermans parameter, S_2, to higher-order anisotropy parameters and benchmarking their evolution against a generalized Maier-Saupe-type anisotropy distribution function, we show that higher-order anisotropy parameters qualitatively distinguish alignment regimes that are indistinguishable from S_2 alone. The work establishes linker topology as a controlling variable for multiscale flow alignment in CNC systems and highlights the higher-order character of their alignment behavior.

1. Introduction

The surface modification of cellulose nanocrystals (CNCs) is a key strategy for tailoring their colloidal stability, rheological response, self-assembly behavior, compatibility with polymer matrices, etc[1–4]. This versatility arises from the array of reactive surface groups, primarily hydroxyl (-OH) functionalities and, in sulfuric acid hydrolyzed CNCs, negatively charged sulfate half ester (-OSO_3H) moieties, which provide multiple sites for chemical functionalization. Reported modification routes include the physical adsorption of surfactants, polymers, or nanoparticles; covalent derivatization of hydroxyl groups through esterification, alkylation, or silylation; and the substitution of charged or reactive sulfate groups [1,3,5–7]. Notably, the substitution of sulfate groups enables conjugation reactions to proceed in aqueous media rather than organic solvents [1,3]. Börjesson et al. demonstrated that azetidinium salts readily conjugate to the CNC sulfate groups, providing a straightforward, water-based route to hydrophobized CNCs [8]. One of the significant consequences of this modification is the suppression of acid-catalyzed thermal degradation, as the conversion of sulfate half-esters to covalently bound diesters stabilizes the CNC surface [9,10]. Building on this approach, subsequent work by Westman and co-workers examined the synthesis and dispersion rheology of such conjugated CNCs [11], their role as polymer reinforcements [9], their influence on nonlinear rheology [12] and shear-induced birefringence [13].

Controlling multiscale structural alignment is paramount for defining the macroscopic properties of CNC based material systems, e.g. in the form of films [14,15]. Among the external fields capable of inducing order, magnetic, electric, or flow fields, the latter are by far the most relevant for manufacturing operations [16]. Consequently, understanding how surface modification affects flow-induced order and the resulting rheological response remains central to optimizing the preparation and properties of CNC-based materials. In viscometric flows,

* Corresponding author.
E-mail addresses: westman@chalmers.se (G. Westman), roland.kadar@chalmers.se (R. Kádár).
[1] These authors contributed equally to this work.
[2] These authors contributed equally to this work (secondary equal contribution).

https://doi.org/10.1016/j.jcis.2026.140913
Received 2 February 2026; Received in revised form 1 June 2026; Accepted 8 June 2026
Available online 13 June 2026

rheological response functions inherently couple mechanical deformation with structural evolution, providing insight into particle dynamics and flow-structure interactions [17].

However, flow-induced alignment in CNC suspensions is intrinsically multiscale. Individual nanocrystals, typically tens to hundreds of nanometers long, rarely exist as isolated rods: they associate into bundles and aggregates [18] and, at higher concentrations, self-assemble into chiral nematic (cholesteric) mesoscale domains. These domains range from tactoids, where the intra-domain order is uniform, to larger formations with complex alignment configurations [19]. In the present work we focus on biphasic systems, where isotropic and cholesteric domains coexist. Any realistic description of alignment must therefore span hierarchical levels from single particles to micrometer-scale tactoids [20,21]. Although rheological material functions are highly sensitive to microstructural changes, they represent a stochastic average of all spatiotemporal interactions within the sample.

Experimentally, the hierarchical nature of pristine, sulfate-stabilized CNCs in aqueous media systems has been interrogated using complementary optical and scattering techniques, including flow birefringence and polarized-light imaging (PLI) [22–28], small-angle light scattering (SALS) [25,29], small-angle neutron scattering (SANS) [30], and small-angle X-ray scattering (SAXS) [29,31]. Overall, previous studies have converged towards a sequence of flow-induced structuring regimes. Without claiming universality, it is generally accepted that at low shear rates, large cholesteric domains progressively align with their helical axes perpendicular to the flow direction while preserving their pitch. At intermediate shear rates, micrometer-sized tactoids fragment into smaller elongated domains, whose size falls below the pitch length, resulting in the apparent loss of the cholesteric signature. And finally, at even higher shear rates complete breakup of tactoids and orientation of individual CNCs parallel to the flow, producing a nematic-like arrangement and further shear thinning [29,30].

In laminar flow between parallel plates (torsional flow), alignment can be detected by polarized light imaging (PLI) through the appearance of the characteristic Maltese-cross pattern. The Maltese cross is a birefringence pattern observed under crossed polarizers when anisotropic domains develop orientational order, appearing as four alternating bright and dark quadrants due to the dependence of transmitted light intensity on the orientation of the optical axes relative to the polarizer directions. In CNC suspensions, this pattern indicates collective alignment of birefringent CNC domains and mesoscale structural organization, reflecting a predominant alignment of optical indicatrixes in the flow direction [32,33]. Recent combined Rheo-PLI-SAXS experiments have shown that the onset of the Maltese cross, whereby the aligned optical indicatrixes were assigned to the mesoscale, does not necessarily coincide with nanoscale alignment [31,34]. It was proposed that this decoupling likely arises from the distinction between the alignment of mesoscale domains and the alignment dynamics of their internal nanoscale structure [31]. A conjugated azetidinium-modified CNC suspension of the type C_m-N-C_n-Prop-2-OH-CNC, where $\{m, n\}$ is number of carbons in the alkyl chains, was used in the study as an example where the liquid crystalline order is being disrupted. Mesoscale orientation was detected over one decade in shear rate earlier than orientation at nanoscale. This was not further explored and, overall, the matter of propagation of alignment across lengthscales in the flow of surface modified CNCs remains to be addressed in the scientific literature. Earlier studies on similar surface architectures using a combination of rheology and PLI showed that only linear/asymmetric C_{11}-N-C_1 linkers exhibited pronounced flow-induced birefringence, whereas branched/symmetric C_6-N-C_6 system suppressed alignment. The results were explained based on molecular dynamics simulations primarily in terms of linker mobility [13].

Here we extend conjugated surface CNC modifications to a systematic Rheo-PLI-SAXS study aimed at resolving how linker topology controls multiscale flow alignment. We examine a controlled series of C_m-N-C_n-Prop-2-OH-CNC architectures with $\{m, n\} \in \{\{2,2\}, \{6,1\}, \{6,6\}\}$. This work makes three main advances over previous studies. First, in contrast to our prior proof-of-principle Rheo-PLI-SAXS work that established the technique on a single conjugated example [31], we obtain a structure-property dependence across a series of linker topologies rather than a single observation, which allows the mesoscale to nanoscale alignment decoupling to be interpreted rather than merely reported. Second, we show that the magnitude and qualitative shape of the decoupling depend strongly on linker symmetry and size, identifying topology as a controlling variable for the propagation of alignment across lengthscales in surface-modified CNCs. Third, we extend the orientational order analysis beyond the Hermans S_2 parameter to include S_4 and S_6, and we benchmark the experimental (S_4, S_6) evolution against a generalized Maier-Saupe-type orientational distribution function shown to describe nematic colloidal systems [16]. The higher-order trajectories distinguish alignment regimes that are indistinguishable by S_2 alone, and reveal that the modified CNC systems deviate systematically from the unimodal nematic predictions that fit the pristine reference above a critical shear rate. This indicates that their flow-induced alignment not only does not follow the same sequence of physical processes as the pristine reference, but also appears to depend on the surface linker topology, despite the similarity in S_2.

2. Experimental section

2.1. Cellulose nanocrystals and surface modified cellulose nanocrystals

A 4 wt% CNC suspension was prepared by dispersing 4 g of CNC powder (CelluForce, Canada) in deionized (DI) water (96 mL) under magnetic stirring for 2 h. The preliminary dispersion was subsequently probe-sonicated using an Ultrasonic Processor VC505 equipped with a 1/2″ microtip, operating at 500 W with an amplitude of 40% and a frequency of 20 kHz for 10 min, corresponding to an energy input of 6.25 J mL^{-1}. Sonication was continued until a visually clear and homogeneous suspension was obtained.

From this point onward, the procedure followed that described in our previous publications [12,13,31]; therefore, only a brief summary of the key steps is provided here. The following azetidinium salts were synthesized for conjugation to the sulfate half-ester groups (-OSO_3H) on the CNC surface:

- 3-hydroxy-1-ethyl-1-ethylazetidin-1-ium chloride (C_2-N-C_2-Prop-2-OH; abbrev. C_2-N-C_2)
- 3-hydroxy-1-methyl-1-hexylazetidin-1-ium chloride (C_6-N-C_1-Prop-2-OH; abbrev. C_6-N-C_1)
- 3-hydroxy-1-hexyl-1-hexylazetidin-1-ium chloride (C_6-N-C_6-Prop-2-OH; abbrev. C_6-N-C_6)

Here, we use the term topology to refer specifically to the configuration of the surface linkers. Although two of the systems share the same branched topology, this terminology is adopted to avoid confusion with filler morphology, defined here as the CNC core dimensions and shape, which remain minimally altered across all samples. The surface sulfate density of the CelluForce CNCs used in this study was estimated at ~330 μmol/g based on conductometric titration of sulfuric-acid-hydrolyzed CNC reported in our previous work [12], taken as a representative value for this class of material. The azetidinium salts were added on this basis, in a 1:1 molar ratio relative to the surface sulfate groups. The conjugation reaction was carried out at 90 °C for 4 h. The working concentration of the modified suspensions was 4 wt%, identical to that of the parent stock and unchanged by the conjugation and dialysis steps.

Prior to all experiments, the CNC suspensions were re-dispersed by probe sonication using the same protocol described above.

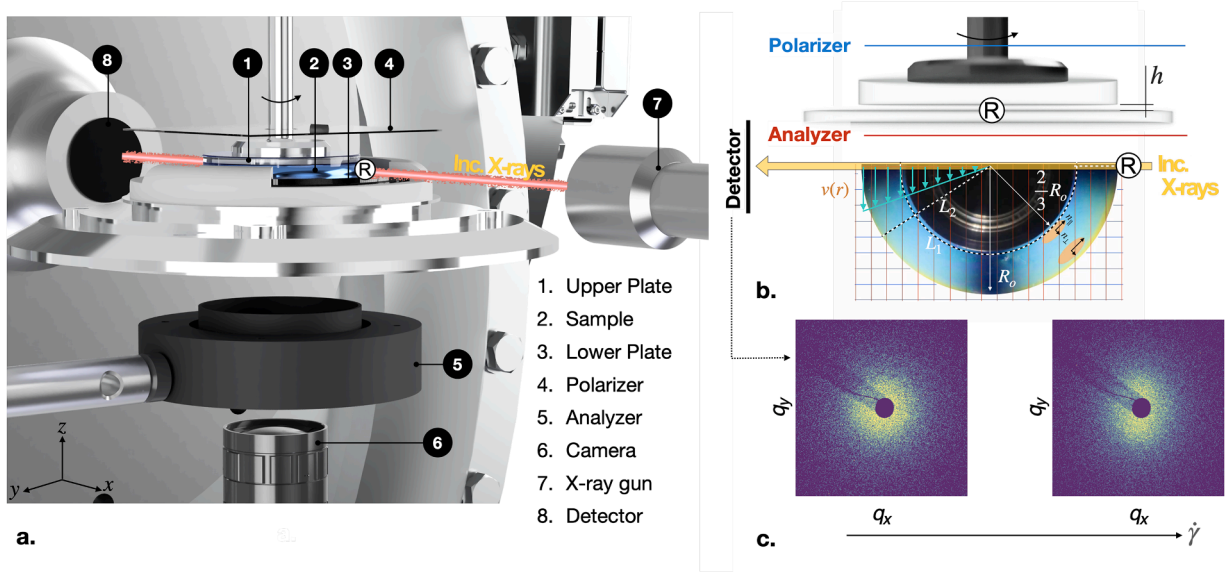

Fig. 1. Rheo-PLI-SAXS experimental setup: (a) schematic overview of the main components of the setup; (b) schematic illustration of the SAXS and PLI measurement geometries shown in two projections: the top view corresponds to the incident X-ray beam (circled R; velocity - velocity gradient plane), while the bottom view corresponds to the optical visualization camera, and illustrates the Maltese-cross pattern; (c) examples of typical SAXS scattering patterns recorded with increasing shear rate. Other notations: L_1 and L_2 are the reference lines.

2.2. Characterization

Fourier Transform Infrared (FT-IR) spectra were recorded using a PerkinElmer Spectrum One FT-IR spectrophotometer (Waltham, MA, US) that included an Attenuated Total Reflectance (ATR; diamond crystal) attachment (GladiATR) from Pike Technologies. Measurements were conducted at room temperature in air and 32 scans in the range of 4000-400 cm^{-1} with resolution of 4 cm. The FT-IR data was normalized, and background corrected.

Thermal gravimetric analysis (TGA) was performed using a TGA/DSC 3+ Star system (Mettler Toledo, Switzerland) to determine the thermal stability of CNC and surface modified CNCs. Samples of 5 mg were weighed and heated from 25 to 500 °C at a rate of 5 °C/min under a nitrogen flow rate of 20 mL/min.

A Zetasizer Nano ZS (Malvern Instruments, UK) was used to measure the zeta-potential. A 50 mW diode-pumped solid-state laser was used as the light source with a wavelength of 532 nm. The concentration of the test samples was 0.1 wt% and their pH was the same. DTS1070 folded capillary cells were filled with each sample and allowed to stabilize for 120 s, repeated 6 times for averaging.

For the construction of space-time diagrams, $2R_o = 43$ mm is the radius of the moving plate, $h = 1$ mm is the measuring gap, $v(r)$ is the velocity distribution on the moving plate and $n_{\parallel}, n_{\perp}$ are the principal axes of the optical indicatrixes depicted (not CNCs). The LED light source of the PLI optical train was placed upstream from the Analyzer and is not represented.

2.3. Rheology combined with polarized light imaging and small-angle X-ray scattering, Rheo-PLI-SAXS

Rheo-PLI-SAXS experiments were conducted at the CoSAXS beamline [35] at the MAX IV synchrotron facility, using a newly developed experimental setup available through the Advanced Rheological Characterization Science Initiative at MAX IV [31,34], see Fig. 1a. The X-ray beam energy at the sample position was 15 keV, and the detector was positioned 3.5 m downstream of the sample. This configuration resulted in a scattering vector range of $q \in [0.007, 0.2]$ $Å^{-1}$, where $q = |\mathbf{q}|$ is the magnitude of the scattering vector.

Rheological measurements were performed using an Anton Paar MCR702 Multidrive (Graz, Austria) operated in a single motor-transducer configuration. The instrument was equipped with a custom transparent bottom plate fixture and a 43 mm diameter standard glass parallel-plate geometry (Anton Paar). Measurements were carried out at a fixed gap of 1 mm and a temperature of 23 °C, maintained using a Peltier-controlled steel ring supporting the bottom glass plate. The transparent geometry provided approximately 7 mm of optically accessible region from the outer radius of the measuring area, enabling simultaneous optical visualization, see Fig. 1b. The total experimental duration was limited to approximately 20 min in order to minimize drying effects, based on preliminary control experiments.

The polarized light imaging (PLI) setup consisted of two linear polarizer films (Edmund Optics, NJ, USA) arranged in a cross-polarized configuration, positioned above (polarizer) and below (analyzer) the rheometer geometry, see Fig. 1a-b. Illumination was provided by a 40W LED light source, and images were acquired using a Canon DSLR camera equipped with a 100 mm macro lens (Canon, Japan), see Fig. 1a. Video acquisition was performed remotely using the Canon EOS Utility software.

2.3.1. Experimental procedures and data analysis

Data synchronization, processing, and visualization were performed using the Multimodal Data Processor and Writer (MuDPaW) v5.8 [36], a custom software framework developed specifically for advanced experiments within the Advanced Rheological Characterization Science Initiative at MAX IV.

The experimental protocol consisted of steady shear tests with predefined steady-state intervals, following procedures established in our previous work [26,31]. SAXS and rheological data acquisition were started approximately at the same time within 1 s error margins. During the steady-state interval, four SAXS scattering patterns were recorded with an exposure time of 0.1 s at an acquisition frequency of 1 Hz. Representative single-shot raw scattering patterns are shown in Fig. 1c.

Following normalization and background subtraction using water as reference, the SAXS data were radially integrated over the full probed q-range. Based on the radially integrated intensity, azimuthal integration was performed around the characteristic interparticle distance identified for the unmodified 4 wt% CNC reference suspension.

Specifically, azimuthal integration was carried out over the range $q \in [1.43, 2.96] \times 10^{-2}$ Å^{-1}; further details are provided in Appendix A.2. The azimuthally integrated SAXS profiles were subsequently averaged during post-processing for each steady-state shear-rate interval prior to computation of anisotropy parameters.

Hermans' anisotropy parameter and higher-order orientational parameters were computed as

$$S_{2n} = \langle P_{2n}(\cos\varphi)\rangle = \int_{-\pi/2}^{\pi/2} P_{2n}(\cos\varphi), w(\varphi), \mathrm{d}\varphi, \tag{1}$$

where $P_{2n}(x = \cos\varphi)$ are even-order Legendre polynomials generated using Rodrigues' formula, Eq. (A.1) (explicit expressions are provided in Eqs. (A.2)-(A.4) in the Supplementary Information). The weighting function $w(\varphi)$ is defined as

$$w(\varphi) = \frac{I(\varphi)\sin\varphi}{\int_{-\pi/2}^{\pi/2} I(\varphi)\sin\varphi, \mathrm{d}\varphi}, \tag{2}$$

with the normalization condition

$$\int_{-\pi/2}^{\pi/2} w(\varphi), \mathrm{d}\varphi = 1. \tag{3}$$

Angle brackets $\langle\cdot\rangle$ denote averaging. The integration limits were selected based on the peak position of the azimuthal intensity distribution, ensuring that the extracted anisotropy parameters are decoupled from the preferential orientation angle [37]. Consequently, $S_2 \in [0, 1]$, where $S_2 = 0$ corresponds to isotropic scattering (random nanostructure orientation), and $S_2 = 1$ represents complete alignment of the nanostructure.

All anisotropy parameters reported in this work are obtained by direct numerical integration of the azimuthal intensity profile. Fitting-based extraction of S_n was used in preliminary data processing for cross-checking but is not used in the reported results, since S_4 and S_6 proved sensitive to fitting details while S_2 did not. While the overall analysis procedure is standard, we note that comparable methodological details are often omitted in the existing literature.

Polarized light imaging (PLI) video data were processed into space-time diagrams by extracting a circular locus of pixels at a radius $r = (2/3)R_o$, corresponding to the geometrical position at which the local shear rate equals the nominal shear rate $\dot{\gamma}$, denoted L_1 in Fig. 1b. This representation captures the onset and evolution of the Maltese-cross pattern at the nominal shear rate. In addition, a radial line of pixels extending across the measurement gap was extracted (denoted L_2 in Fig. 1).

Using the synchronization procedure described in Appendix A.2, steady-state PLI data were converted to the CIELab* color space [38] and temporally averaged. The area under the curve of the azimuthal-angle-averaged color-space norm, $A_{L1} = \sqrt{L^2 + a^2 + b^2}$, was then computed. Reported values were normalized by the corresponding startup value, $A_{\mathrm{norm}} = A_{L1}(\dot{\gamma})/A_{L1}(\dot{\gamma}_{\mathrm{min}})$. Representative PLI frames extracted at selected shear rates for all samples are provided in Fig. A.8. Additional details of the PLI data analysis are given in Appendix A.2.

3. Results and discussion

First we outline data supporting the successful completion of the CNC surface modification reactions. Thereafter, we focus on the multiscale analysis of the suspensions followed by a discussion of the higher order anisotropy parameters.

3.1. Grafting of azetidinium salts

Thermogravimetric analysis confirms the successful surface modification of pristine CNC, Fig. 2a. The observed mass loss shows that azetidinium-functionalized samples resist thermal degradation markedly longer than pristine CNC. Quantitatively, derivative thermogravimetric (DTG) analysis (Fig. 2b) shows the maximum degradation rate for untreated CNC at 186.4 °C, whereas the grafted samples exhibit an increase of approximately 50-62 °C in thermal stability after surface modification. The higher degradation temperatures of the modified CNCs is technologically advantageous, as it is in the processing range of many polymers [39]. The thermograms exhibit two-region characteristics, where the modified CNCs show a reduced expression of the rapid, acid-catalyzed pyrolysis attributed to sulfate half-esters, followed by a more gradual carbonization of the residue. The DTG further supports this interpretation by revealing a broader, lower-temperature degradation profile for pristine CNC and sharper, shifted decomposition peaks for the grafted samples, indicative of altered degradation pathways after functionalization. Moreover, differences in residual mass at 500 °C between pristine and modified CNCs is consistent with the elimination or neutralization of thermally unstable -OSO_3H moieties.

Table 1
Zeta potential.

Sample	Zeta Potential [mV]	
	Mean	Std. Dev.
CNC	-38.3	1.46
C_2-N-C_2-Prop-2-OH-CNC	-37.8	1.97
C_6-N-C_1-Prop-2-OH-CNC	-39.3	0.37
C_6-N-C_6-Prop-2-OH-CNC	-36.1	1.86

In the FT-IR spectra (Fig. 2b), a broad absorption spanning 3600 to 3000 cm^{-1} is assigned to hydrogen-bonded O-H stretching from the abundant hydroxyl groups on the glucopyranose units. The region 3000 to 2900 cm^{-1} features aliphatic C-H stretching (asymmetric and symmetric, CH_2/CH_3) arising from the cellulose backbone and, in the modified samples, from the appended propyl-2-hydroxy-dialkyl chains. Water retained in the films contributes a band near 1640 cm^{-1} corresponding to H-O-H bending. In the fingerprint region, the polysaccharide framework yields the expected C-O and C-O-C vibrations, including the diagnostic (β)-1,4-glycosidic C-O-C mode at ~ 901 cm^{-1}, which confirms the cellulose connectivity. A distinct feature around 814 cm^{-1} is attributed to C-O-S vibrations associated with sulfate half-ester/diester groups on CNC surfaces.

Covalent surface functionalization at the half-sulfate ester sites with azetidinium salts perturbs these signatures in predictable ways. The modified spectra show higher intensity of the C-H stretching band near 2850 cm^{-1}, consistent with the increased methylene content introduced by the grafted alkyl moieties. Concomitantly, the sulfate-related band undergoes a subtle downshift from ~ 814 to ~ 808 cm^{-1}, suggesting a change in the local bonding environment of the C-O-S group upon substitution. Such subtle spectral variations are expected, considering that the glucose-to-azetidinium ratio is approximately 20:1. This would result in a comparatively weak signal contribution from the modified sulfate groups. In addition, overlapping vibrational modes and different sulfate conformations make distinct peak shifts difficult to resolve. The FT-IR data should therefore be regarded only as evidence complementary to the enhanced thermal stability observed in the TGA analysis. As such, the FT-IR results support successful surface modification of the CNCs, while the persistence of the β-1,4 linkage band confirms that the cellulose backbone remains intact. These results are consistent with the substitution of protonated sulfate groups and have been reported previously as a reliable indicator of successful CNC surface modification in our earlier studies [12,13,31].

Zeta potential measurements (Table 1) confirm that the surface modification did not alter the colloidal stability. The similarity in zeta potential before and after azetidinium conjugation suggests that the effective electrostatic environment at the slipping plane remains largely unchanged, despite chemical modification of the CNC surface. This indicates that the surface modification does not substantially alter the long-range electrostatic stabilization of the suspensions, while allowing for significant changes in short-range interactions and thermal stability. This is further emphasized in the Rheo-PLI-SAXS results below. The current findings contrasts with a previous study on

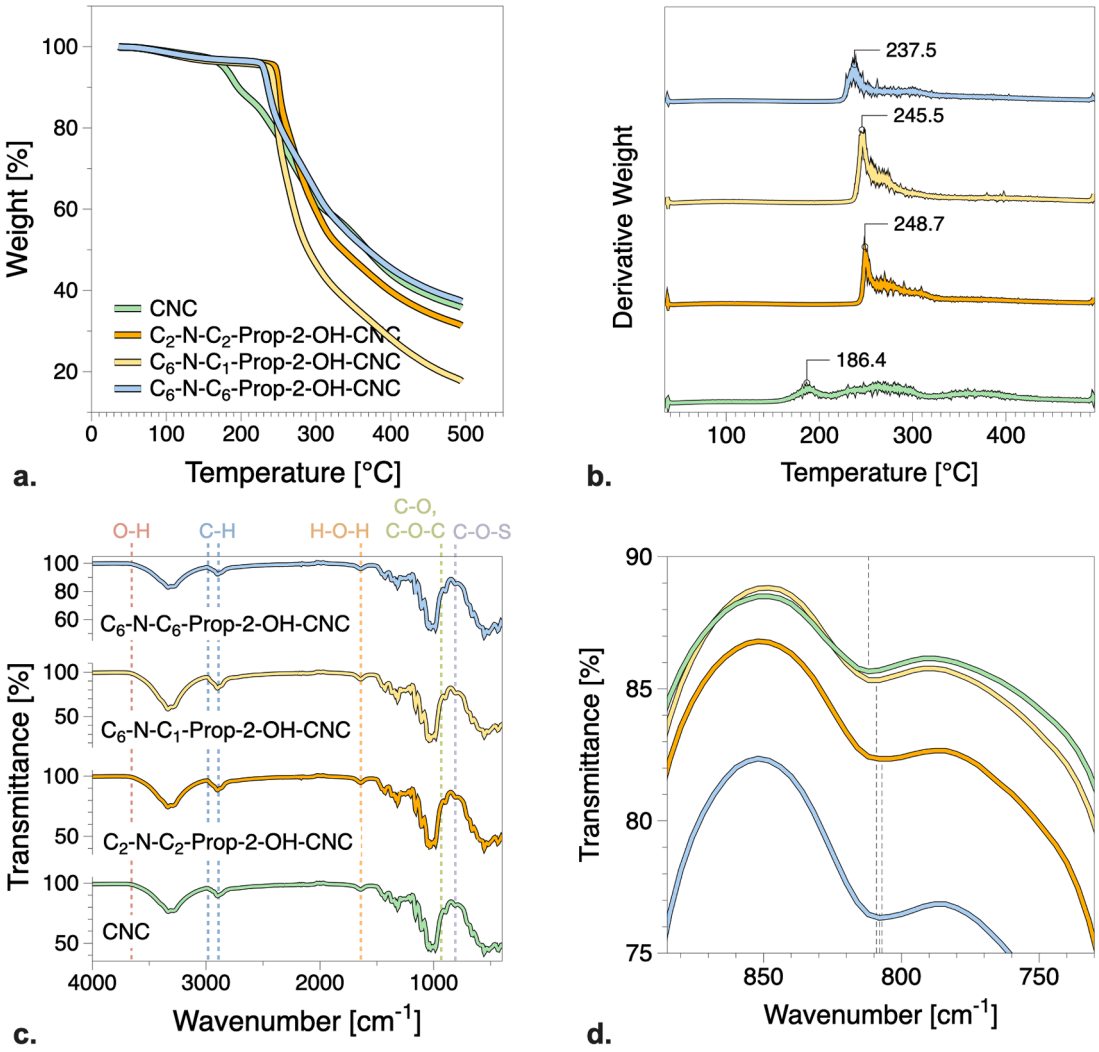

Fig. 2. (a) Thermogravimetric analysis (TGA) of pristine CNC and azetidinium-functionalized CNCs, showing enhanced thermal stability and delayed onset of degradation after surface grafting. (b) Derivative thermogravimetric (DTG) curves highlighting shifts in the main decomposition temperatures upon functionalization. (c) FT-IR spectra of pristine CNC and modified CNC samples, confirming successful grafting through the appearance and evolution of characteristic functional-group vibrations associated with azetidinium moieties. (d) Expanded view of the FT-IR spectra in the 890-730 cm^{-1} region.

surface-grafted CNCs for polymer composites[9], where a significant decrease in zeta potential was reported. This discrepancy is likely due to differences in the sulfate content of CNCs following autocatalyzed desulfation.

3.2. Multiscale analysis

Before discussing the results, it is important to estimate the noise level in S_2, below which we consider the nanoscale alignment to be random. In this study, we use the C_6-N-C_6 dataset as a reference, since its azimuthal integrations show no evidence of nanoscale alignment below 100 s^{-1}, see Fig. A.7a. Based on this reference, the cutoff was set to $S_2 = 0.027$ for these datasets, Fig. A.7b.

As context for the multiscale data discussion, it is useful to consider a simple kinematic argument based on the shear-rate distribution across the rheometer gap, $\dot{\gamma}(r) = v(r)/h$, see Fig. 1b. In the parallel-plate geometry used here, the local shear rate increases monotonically with radial position, from $\dot{\gamma}(r = 0) = 0$ at the center to a maximum value at the outer edge, $\dot{\gamma}(r = R_o)$. Consequently, regions closer to the outer radius experience higher shear rates than the nominal value evaluated at $r = 2/3\ R_o$. Importantly, in the radial-incident configuration the SAXS X-ray beam probes across this shear-rate gradient and therefore integrates contributions from regions experiencing a range of local shear rates. In contrast, both the rheological measurements and the PLI signal—used here to monitor the onset of the Maltese-cross pattern—are evaluated at $r = 2/3\ R_o$. It is therefore expected that an increase in the Hermans anisotropy parameter, S_2, would be detected at nominal shear rates greater than or equal to those corresponding to the appearance of the Maltese-cross pattern, i.e. $\dot{\gamma}^{SAXS}_{orien} \geq \dot{\gamma}^{PLI}_{orien}$. The equality corresponds to the limiting case in which an incremental increase in the imposed nominal shear rate first induces structural alignment only in the outer region of the gap, $r \in [2/3\ R_o.\ R_o]$.

The multiscale plots in Fig. 3 compare the viscosity functions (top panels), the normalized data under the imaging data, overlaid on the PLI space-time diagrams (middle panels), and the Hermans anisotropy parameter, S_2, overlaid on the steady-state azimuthal integration data (bottom panels). The S_2 datapoints reflect the magnitude of S_2, i.e. a circle corresponds to $S_2 \approx 0$ (isotropy) whereas ellipsis symbols indicate measurable nanoscale anisotropy. The principal axis of the ellipses (black line inside the datapoints) represent the reals space preferred nanoscale alignment direction, see Fig. A.6.

In the multiscale analysis presented below, SAXS data points are represented as quasi-indicatrixes (Fig. A.6). A circular symbol corresponds to random nanoscale alignment (isotropy), as defined by the

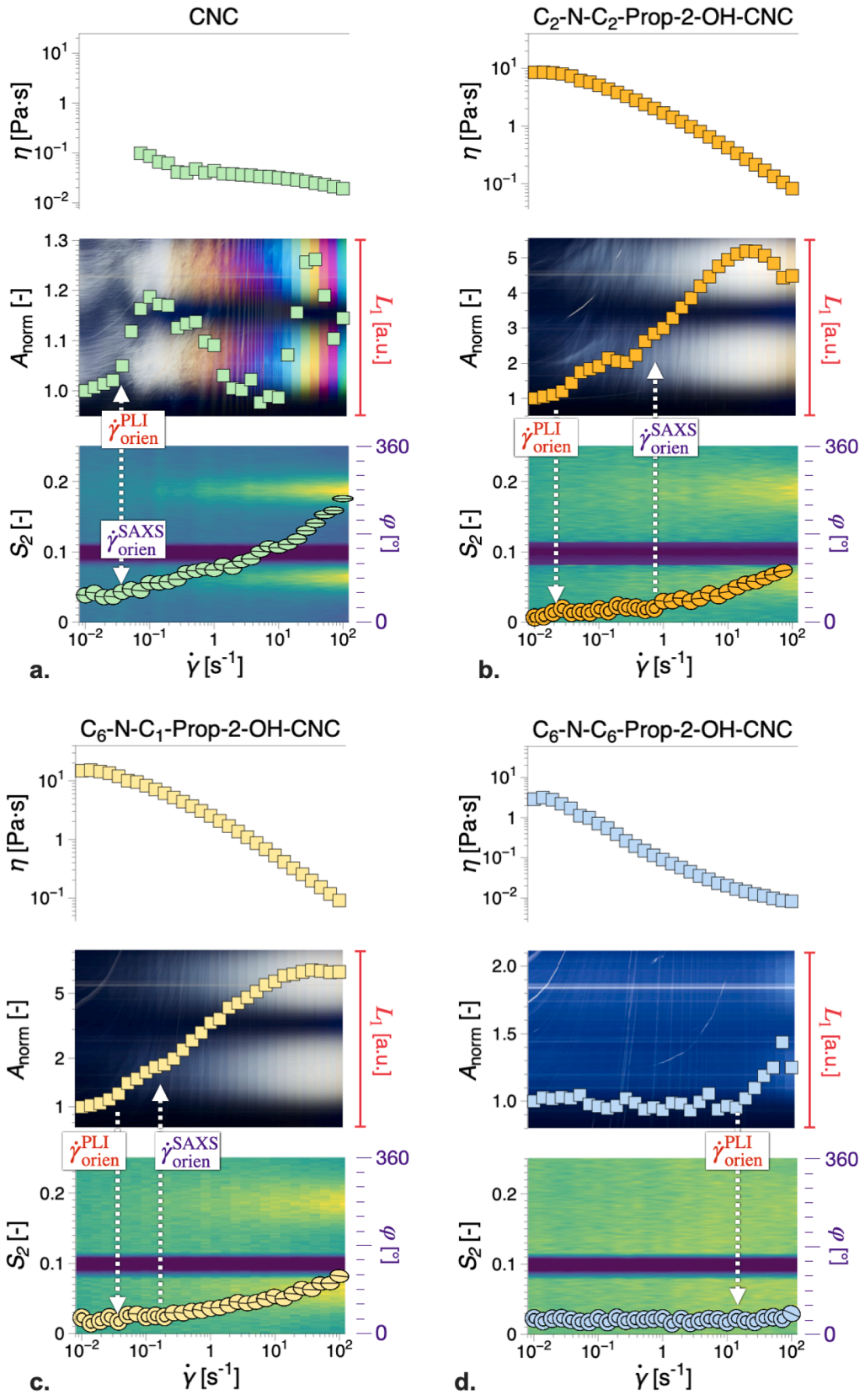

Fig. 3. Multiscale analysis comprising (top panels) the bulk rheological material response, $\eta(\dot{\gamma})$, (middle panels) quantification of mesoscale orientation through the normalized area under the imaging data, $A_{norm}(\dot{\gamma})$, overlaid with a space-time diagram along arc L_1, see Fig. 1 and A.2, (bottom panels) and Hermans' anisotropy parameter, $S_2(\dot{\gamma})$, overlaid on the corresponding azimuthal integration from SAXS, where φ is the azimuthal angle.

cutoff value, whereas oval-shaped symbols indicate measurable nanoscale anisotropy. In the latter case, the orientation of the principal axis of the ovals represents the nanoscale preferred alignment angle in real space.

The reference 4 wt% CNC suspension provides an example for which the critical shear rates for nanoscale and mesoscale alignment coincide, Fig. 3a. Up to $\dot{\gamma}_{\text{orien}} \approx 0.06 - 0.1\ s^{-1}$, birefringent regions can be observed in PLI, see the extracted video frames in Fig. A.8, consistent with a relatively low and nearly constant level of preferential alignment in the flow direction inferred from SAXS. This behavior implies the presence of chiral nematic domains whose optical axes are preferentially oriented perpendicular to the flow direction [29]. Above this critical shear rate, a 'Maltese-cross' pattern is detected in PLI approximately accompanied by an increase in the Hermans orientation parameter S_2. This transition is consistent with previous observations on biphasic CNC systems prepared using similar protocols [31]. Notably, in our earlier study the 4 wt% CNC suspension–derived from the same supplier but from a different stock–also exhibited coincident critical alignment shear rates, yet at a substantially higher shear rate, $\dot{\gamma} \approx 0.4\ s^{-1}$. While the reason for this discrepancy remains unresolved, the necessity for a simultaneous consideration of nano and meso lengthscales to elucidate the multiscale alignment of such hierarchical systems is thus emphasized. The viscosity function of the reference 4 wt% CNC suspension exhibits the characteristic three-regime behavior, with the onset of coupled alignment across length scales occurring already in the first regime. This regime has previously been associated with large-scale aggregate reorganization and restructuring [21,29,30].

In contrast, the surface-modified samples show neither birefringence in PLI nor measurable nanoscale alignment in SAXS in the small-$\dot{\gamma}$ regime, see Fig. 3 and also Fig. A.8. Consistent with this observation, polarized optical microscopy (POM) analyses of comparable surface-modified CNC suspensions have likewise reported an absence of birefringence [13,31]. This would suggest that no local multiscale order is present in the modified samples at rest (no flow) or very low shear rates. An alternative interpretation is that local ordering of CNCs may still occur, but remains insufficient to generate detectable birefringence at the spatial resolution of the PLI measurements. If such locally ordered domains are randomly oriented when averaged along the X-ray beam path, the resulting SAXS signal would correspond to $S_2 \approx 0$, consistent with the absence of a birefringent response. The corresponding viscosity functions of the surface-modified samples show a pronounced increase in magnitude compared to the reference suspension. As shown previously, this behavior reflects the formation of a percolated network mediated by the surface modification [12,13], see also the direct comparison of viscosity functions in Fig. A.7c. The three-region viscosity behavior in pristine CNC suspensions has been associated in the literature variously with biphasic and with liquid-crystalline phases, and is sensitive to sample preparation; it is a persistent but not universal feature of CNC steady-shear viscosity curves [21]. The reference 4 wt% CNC suspension here is consistent with the biphasic case at the studied concentration. For the surface-modified samples, the absence of the three-region behavior is not necessarily straightforward to interpret without further structural information. The difference between the two could therefore reflect a change in the underlying structural state imposed by the linker chemistry, rather than a simple suppression of liquid-crystalline ordering.

As the shear rate is increased, flow-induced alignment is detected in both SAXS and PLI. However, for all surface-modified samples, the onset of the Maltese-cross pattern in PLI systematically precedes the detection of nanoscale orientation in SAXS, such that $\dot{\gamma}_{\text{orien}}^{\text{SAXS}} > \dot{\gamma}_{\text{orien}}^{\text{PLI}}$, see Fig. 3b-c. This observation is particularly striking given that, over the shear-rate interval $[\dot{\gamma}_{\text{orien}}^{\text{PLI}}, \dot{\gamma}_{\text{orien}}^{\text{SAXS}}]$, $S_2 \approx 0$. Both the critical shear rates and the width of the intermediate shear-rate regime appear to be strongly surface topology-dependent. The suspension with short, symmetric chains (C2-N-C2) exhibits a Maltese-cross pattern at $\dot{\gamma}\text{orien}^{\text{PLI}} \approx 0.02\ s^{-1}$, whereas measurable nanoscale alignment in SAXS is only detected at substantially higher shear rates, $\dot{\gamma}\text{orien}^{\text{SAXS}} \approx 0.8\ s^{-1}$. In contrast, the asymmetric C6-N-C1 sample shows $\dot{\gamma}\text{orien}^{\text{PLI}} \approx 0.035\ s^{-1}$ and $\dot{\gamma}\text{orien}^{\text{SAXS}} \approx 0.18\ s^{-1}$, resulting in a considerably narrower shear-rate interval between mesoscale and nanoscale alignment. Notably, the onset shear rate for mesoscale orientation, $\dot{\gamma}_{\text{orien}}^{\text{PLI}}$, is comparable for both topologies and close to that of the reference CNC suspension, identifying C_6-N-C_1 as the surface-modified system that is qualitatively most similar to the unmodified CNCs. In contrast, the branched C_6-N-C6 sample exhibits mesoscale orientation only at much higher shear rates, $\dot{\gamma}\text{orien}^{\text{PLI}} \approx 11\ s^{-1}$, with no clearly discernible onset of nanoscale alignment in SAXS within the shear-rate range investigated.

Such a propagation of orientational order across length scales–where mesoscale alignment precedes detectable nanoscale alignment–has also been reported in our previous work [31]. The working microstructural picture that has emerged so far from previous Rheo-PLI-SAXS studies is that the coupling or decoupling of alignment across length scales reflects distinct multiscale dynamics of biphasic CNC domains. Highly sonicated suspensions under shear comprise liquid crystalline domains prone to elongation under shear, thereby constraining CNC self-assemblies with their chiral nematic axes preferentially oriented perpendicular to the flow direction [29]. In contrast, bath-sonicated samples, which contain a higher fraction of aggregates or agglomerates, exhibit mesoscale domains that orient in the flow direction with effective domain refractive indices, yet without long-range nanoscale orientational coherence across domains. This comparison suggests that the elasticity of domains composed predominantly of well-dispersed, pristine CNCs–such as those produced by probe sonication–facilitates domain elongation and, in turn, constrains local nanoscale order. Conversely, in domains containing significant fractions of bundles or aggregates, elongation is either hindered or requires additional deformation to induce intra-domain ordering.

For the present surface-modified CNC suspensions, pristine sulfate-stabilized CNCs at low ionic strength serve as a useful reference, as they are well described as purely repulsive colloids. Grafting azetidinium salts onto the CNC surface results in an interaction potential that is no longer strictly repulsive but acquires weak, orientation-dependent attractive contributions. The absence of birefringence at low shear rates, together with the decoupling between mesoscale and nanoscale critical alignment shear rates, suggests that aggregates or locally heterogeneous structures may disrupt self-assembly at rest but can be partially reorganized under shear. Such reorganization could give rise to shear-induced birefringence and, at sufficiently high shear rates, to detectable nanoscale orientation. While this points to alignment scenarios that differ fundamentally from those of the reference CNC suspension, the present results do not yet establish a definitive mechanism for multiscale alignment in the surface-modified systems. Nevertheless, a clear dependence on linker topology emerges. More linear surface modifications favor nanoscale alignment, potentially due to enhanced segmental mobility, as previously proposed [13]. Interestingly, very short branched topologies (C_2-N-C_2) display behavior that is qualitatively similar, suggesting that both mobility and steric constraints play a role.

While intriguing, these observations leave open the question of the sequence of processes governing the propagation of alignment and structuring across length scales under flow in surface-modified CNC suspensions. To investigate this further, we next examine the radially resolved scattering data, followed by an analysis of higher-order anisotropy parameters.

3.3. Radial integration analysis

Based on the radially integrated shear-rate-averaged SAXS data presented as Kratky plots in Fig. 4a, in agreement with previous studies, this characteristic length scale remains essentially invariant with shear rate over the range investigated [29], as shown in Fig. 4b, despite the expected breakup of chiral nematic domains and their subsequent fragmentation under flow. While the peak position remains unchanged, the radially integrated intensity for the unmodified CNCs increases slightly

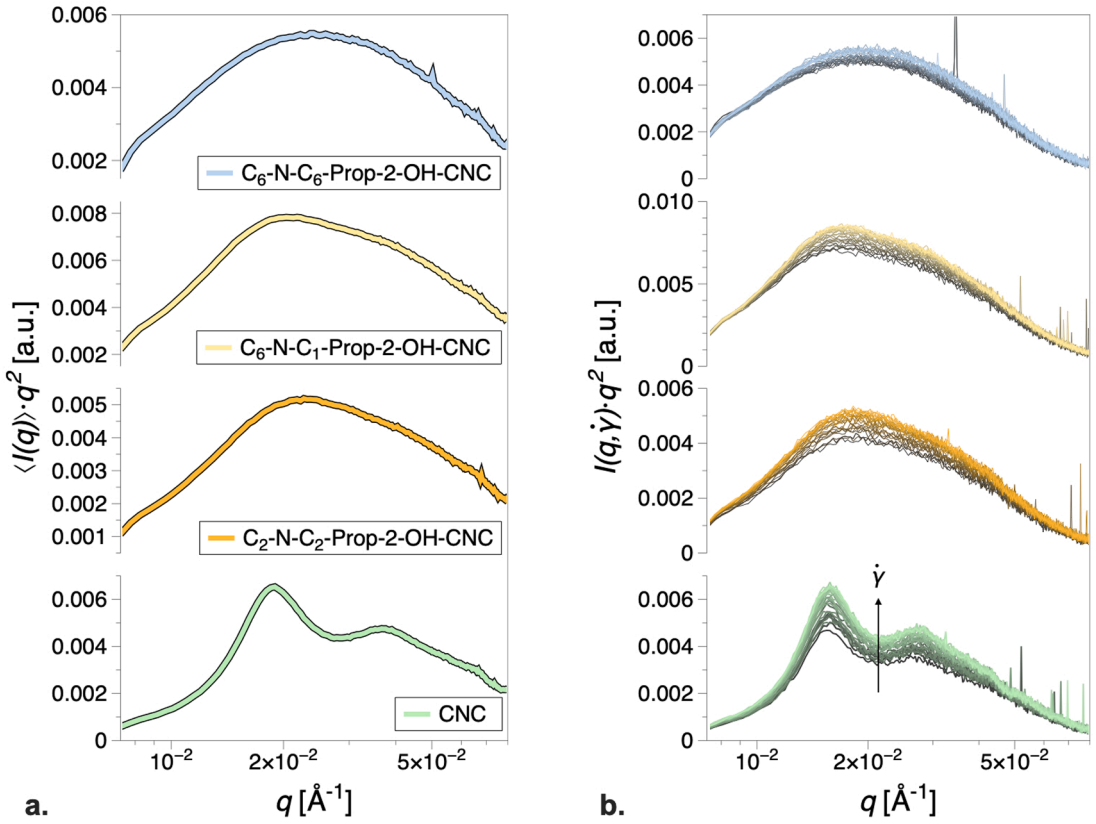

Fig. 4. Radial integration analysis: (a) Kratky representation of the scattering intensity, $I(q)$ as function of the scattering vector magnitude $q = |\mathbf{q}|$, averaged over all shear rates investigated, for the pristine CNC reference and the three surface-modified suspensions. (b) Evolution of the radially integrated $I(q)$ with increasing shear rate for each sample. The radial integration is performed over the entire azimuthal range of the scattering data.

with shear, consistent with weak nanoscale orientational ordering without a change in the average interparticle spacing.

Fig. 4a shows that the overall shear-rate-averaged radial scattering profiles, averaged over all shear rates, exhibit only maximally weak sensitivity to shear with shape and peak positions that are essentially preserved throughout the tests, similar to the unmodified CNCs. In particular, C_2-N-C_2 and C_6-N-C_1 show only weak shear dependence of the radially integrated scattering curves, Fig. 4b, above shear rates that correspond to the onset of alignment. In addition to the position of the peak, the radial scattering profiles also differ in their breadth between pristine and modified CNCs. The pristine reference exhibits a comparatively well-defined peak position, consistent with a relatively narrow distribution of inter-particle distances. The modified samples display visibly broader peaks (Fig. 4), indicating a wider distribution of inter-particle distances and a less-defined characteristic length scale.

Despite their substantially higher shear viscosities, the surface-modified suspensions exhibit characteristic interparticle distances that are consistently smaller than those of the reference CNCs when averaged over all shear rates. Approximately 27 nm for C_2-N-C_2, 31 nm for C_6-N-C_1, and 25 nm for C_6-N-C_6, compared to 34 nm for the reference CNC. The shorter characteristic interparticle spacing observed for the surface-modified systems likely reflects weak particle alignments with shear which in turn alters their packing. In this sense, the reduced interparticle distances observed for the surface-modified suspensions would indicate a denser local organization induced via azetidinium conjugation. The combination of dense local packing and weak shear dependence of the radially integrated SAXS curves, particularly pronounced for C_6-N-C_6, is consistent with a locally compact yet largely disordered nanoscale structure that is resistant to shear-induced nanoscale reorganization. This further corroborates the absence of detectable nanoscale (intentionally emphasized) alignment, as quantified by S_2 and with the strongly delayed onset of mesoscale alignment observed by PLI for this sample. When directly comparing the shear rate dependent evolution of S_2 and normalized maximum peak scattering intensity, $I(q)$, on shear rate, it appears that for surface modified samples, even at the relatively low S_2 attained, there is a significant change in the structural correlation lengthscale.

3.4. Higher-order anisotropy parameters

At this point, a natural question needs to be addressed: what do these higher-order parameters represent? SAXS probes a two-dimensional projection of an *a priori* unknown three-dimensional orientational distribution function (ODF), expressed experimentally by the azimuthal dependence of the scattered intensity. Subtle changes in the shape of the underlying ODF, such as peak sharpening, shoulder formation, or increased heterogeneity, can therefore manifest in the extracted anisotropy parameters. In this context, S_4 primarily reflects deviations from a simple unimodal distribution, such as peak sharpening versus shoulder-dominated angular profiles, whereas S_6 acts as a higher-order descriptor sensitive to finer distribution features, including tail weight and subtle shape heterogeneity beyond peak sharpening, see Fig. A.10 and description thereof in the Supplementary information. It is important to note that the absolute magnitudes of S_4 and S_6 depend on details of the analysis procedure, including the use of fitted functions as input to the S_n algorithm and the degree of smoothing applied to the azimuthal intensity profiles. However, qualitatively, the results are very similar within such variations, particularly as long as smoothing is limited to suppressing high-frequency noise and when peak maxima and positions are preserved. For the present experiments, the motivation for examining higher-order parameters arises from the observation that the fourth- and sixth-order anisotropy parameters, S_4 and S_6, display markedly different shear-rate

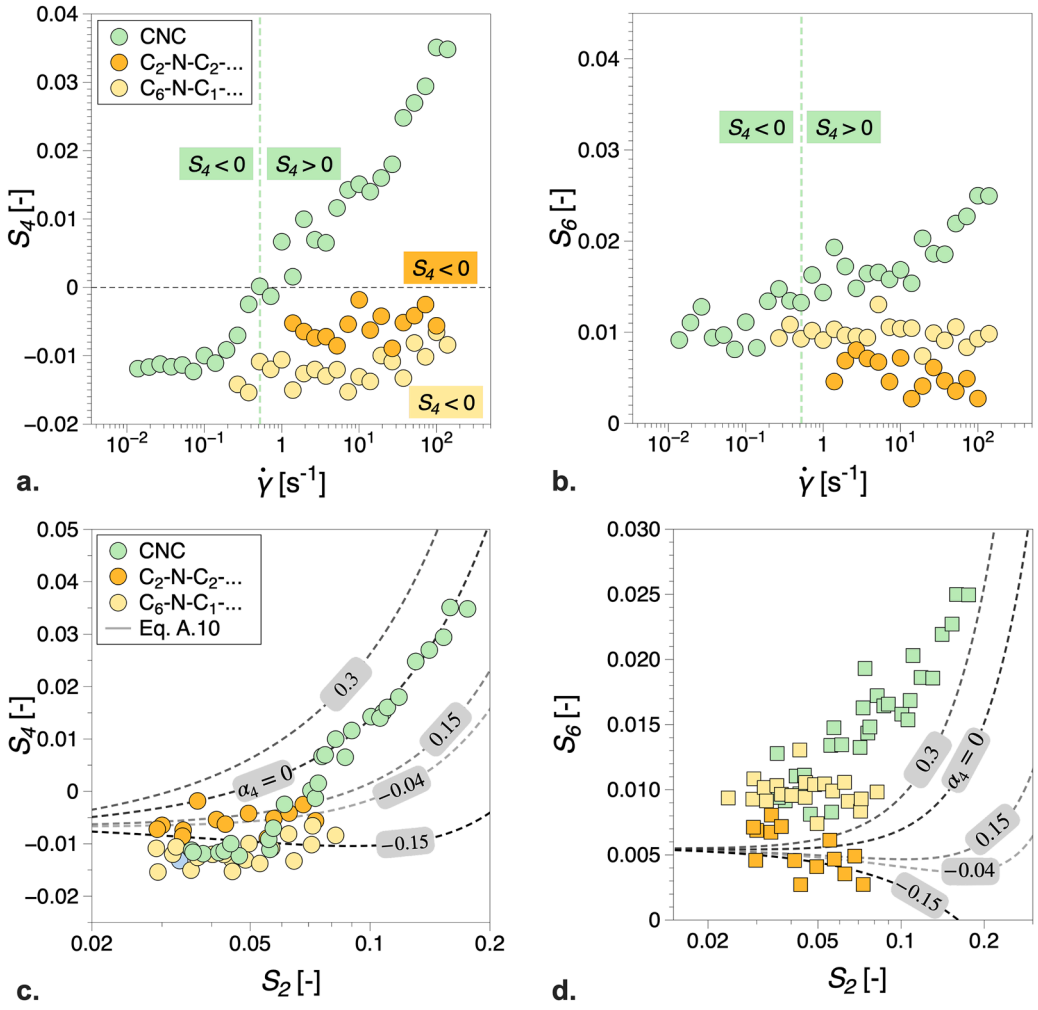

Fig. 5. Evolution of higher-order anisotropy parameters with shear rate: (a) S_4, which primarily reflects peak sharpening versus shoulder-dominated angular distributions (kurtosis-like behavior), and (b) S_6, which acts as a higher-order measure sensitive to finer distribution features such as tail weight and subtle shape heterogeneity beyond peak sharpening. Interdependence of higher-order and the Hermans anisotropy parameter: (c) S_4 vs. S_2 and (d) S_6 vs. S_2. The dotted lines in (c) and (d) were determined based on Eq. (4).

dependencies for the surface-modified samples compared to the reference CNC suspension, Fig. 5a-b.

For the reference CNC suspension, both S_4 and S_6 qualitatively follow the evolution of $S_2(\dot{\gamma})$, exhibiting near-constant values at low shear rates below $\dot{\gamma}_{orien}$, followed by a gradual increase at higher shear rates. Among the surface-modified samples, C_6-N-C_1 shows the most qualitatively similar behavior to the reference CNC in both S_4 and S_6. Notably, however, S_4 for C_6-N-C_1 remains approximately constant at a magnitude comparable to the reference CNC well beyond $\dot{\gamma}_{orien}^{SAXS}$. In contrast, C_2-N-C_2 exhibits an almost shear-rate-independent S_4 across the entire investigated range, albeit slightly higher in magnitude compared to C_6-N-C_1.

The sixth-order parameter S_6 displays a qualitatively different response: both C_2-N-C_2 and C_6-N-C_1 show a weak but noticable decrease in S_6 with increasing shear rate, in stark contrast to the reference CNC suspension. This divergence between the behaviors of S_4 and S_6 already suggests that higher-order anisotropy parameters encode structural information not captured by S_2 alone.

Identifying the material origins of such anisotropy distribution function shape changes as with varying shear rate amounts to a challenging task and lies beyond the scope of the present work. Nevertheless, a useful comparison can be made by examining the interdependence of higher-order anisotropy parameters relative to S_2. In particular, experimental trends can be compared with reference predictions from classical theoretical frameworks in which the shape of the orientation distribution function (ODF) is uniquely determined by a small number of parameters. One such framework is the Maier-Saupe mean-field theory for nematic liquid crystals [39–42]. To rationalize the relationship between the 2nd (Hermans) and higher-order anisotropy parameters, we consider a generalized Maier-Saupe-type orientational distribution function that allows controlled deviations from a purely unimodal shape and has been extensively validated for nematic liquid crystalline systems [16]:

$$f(\theta) \propto \exp\{m(P_2[cos(\theta)) + \alpha_4 P_4(\cos(\theta))]\} \quad (4)$$

Here, m controls the width of the distribution and thus the magnitude of S_2, while α_4 controls higher-order shape corrections. Further details can be found in Appendix A.4. Within this unimodal ODF family, the higher-order moments S_4 and S_6 are uniquely determined by S_2, leading to well-defined functional dependencies $S_{4,6} = f(S_2)$. We note that θ is here the polar angle of a particle orientation with respect to the director in real space. In using Eq. (4) to determine the anisotropy parameters, we implicitly equate the ODF to the scattered anisotropy distribution function [43]. Thus, although the experimental anisotropy parameters extracted here are derived from azimuthal scattering intensities, comparing normalized higher-order parameters to Maier-Saupe-type predictions could be a simple, yet a potentially powerful tool to assess wether the experimental angular anisotropy analyzed evolves in a manner consistent with a unimodal, nematic-like distribution [44], or whether

additional structural complexity is present. The model in Eq. (4) has been chosen deliberately as the lowest-order extension beyond a pure S_2 description that allows deviations from Gaussian or unimodal alignment. While the orientational distribution is parametrized using a truncated exponential series up to S_4, higher-order parameters such as S_6 are not independently fitted but emerge as predictions of the assumed distribution. Consequently, deviations observed in S_6 are best interpreted as indicators of distribution shape complexity rather than as independent anisotropy parameters [44].

A direct comparison between the experimental data and Eq. (4), illustrating the dependence of higher-order normalized anisotropy parameters on S_2, is shown in Fig. 5c-d. An overview of the generated data and the resulting anisotropy parameters can be additionally found in Fig. A.11. Even within the simplicity of the assumptions above, several intriguing trends can be readily identified. Perhaps the most striking is above $S_2 \gtrsim 0.07$, a simple $\alpha_4 = 0$ prediction captures the experimental $S_4(S_2)$, Fig. 5a, dependence for the reference CNCs. This corresponds to shear rates approximately greater or equal that 2 1/s. This shear rate range appears to include the third region of the reference CNC viscosity curve, see Fig. 3a. This regime has previously been associated with the loss of higher-order hierarchical structures and the dominance of flow-aligned nematic-like order together orienting with this isotropic part of a biphasic system [29,30]. While a final conclusion on predicting the dominance of nematic domains based on S_4 is premature, but very intriguing. For the surface modified systems, C_6-N-C_1 appears to follow the reference CNC behavior for $S_2 < 0.06$, whereas C_2-N-C_2 can be approximately described by the generalized Maier-Saupe model with $\alpha_4 \in (-0.04, 0.15)$. Thus, despite exhibiting similar S_2 values, and shear-induced birefringence patterns, higher-order parameters indicate that C_2-N-C_2 undergoes a distinct multiscale structural evolution under shear, likely reflecting the presence of mesoscale aggregates, consistent with scenarios proposed previously for the de-coupling of alignment across lengthscales [31]. However, $S_6(S_2)$, Fig. 5b., with the possible exception of C_2-N-C_2 none of the parameter choices reproduce the full behavior of the reference CNC suspension, as expected given its chiral nematic structure and expected evolution under shear.

The description above is appealing because physical arguments can be readily made based on the results obtained. While pristine sulfate-stabilized CNCs dispersed at low ionic strength are well described as purely repulsive colloids, grafting of azetidinium groups introduces surface charge heterogeneity and short-range electrostatic correlations. As a result, the interaction potential is no longer strictly repulsive but acquires weak, orientation-dependent attractive contributions.

The modified CNC suspensions differ from pristine CNCs not only in their flow-induced alignment response but also in the nature of the underlying alignment progression itself. Pristine CNCs at the studied concentration display a flow-alignment response consistent with nematic-like ordering beyond a critical shear rate, as expected, and the experimental (S_2, S_4, S_6) agree with the predictions of the generalized Maier-Saupe-type anisotropy distribution function in this regime, Fig. 5c-d. For the modified samples (S_4, S_6) deviate systematically from the unimodal predictions. Taken together, the results suggest that the modified suspensions may not be simply less ordered, but may possess a qualitatively different at-rest microstructure and intrinsic mechanisms to respond to an applied shear field. The modified samples therefore occupy a different region of the orientational anisotropy space than is described by a unimodal nematic alignment state. The magnitude and qualitative shape of the mesoscale-to-nanoscale decoupling, as well as the higher-order anisotropy signatures, depend considerably on linker symmetry and size. However, the results are not consistent with the longest linker arm alone controlling the response, since C_6-N-C_1 shares its longest arm with C_6-N-C_6 but does not behave like it. It is, however, consistent with the previously proposed picture in which segmental mobility of the grafted chains plays a role [13]: in C_6-N-C_1 the asymmetric pairing of a long arm with a short methyl group leaves overall mobility comparable to the short-symmetric C_2-N-C_2 case, whereas in C_6-N-C_6 the symmetric long-armed pairing reduces mobility further. The controlling variable therefore could lie in the combination of symmetry and relative arm sizes, rather than in any single dimensional descriptor. Identification of the specific microscopic mechanism behind this dependence requires complementary characterization beyond the scope of the present work.

4. Summary and conclusions

In this work, we have revisited flow-induced alignment in cellulose nanocrystal suspensions with systematically varied surface architectures using a newly-developed combined rheo-PLI-SAXS experiment. By probing mesoscale optical alignment and nanoscale structural anisotropy simultaneously, we directly assessed how alignment propagates across lengthscales in pristine and alkyl-functionalized CNCs prepared via azetidinium conjugation.

Pristine sulfate-stabilized CNC suspensions (reference) exhibited nearly-identical critical shear rates for mesoscale alignment, as quantified by the onset of the so-called Maltese-cross pattern and nanoscale alignment, as quantified by the Hermans order parameter, S_2. In contrast, all surface-modified suspensions displayed a pronounced decoupling between the lengthscales investigated. The onset of the Maltese-cross pattern in polarized light imaging occurred at substantially lower shear rates than the emergence of measurable Hermans anisotropy in SAXS. The width of this intermediate regime and the absolute values of the critical shear rates were found to depend on the topology of the grafted linker.

While second-order anisotropy parameters alone suggest broadly similar levels of alignment among several surface-modified systems, analysis of higher-order anisotropy parameters revealed qualitative differences in the evolution of angular distribution shapes under shear. In particular, divergent trends in the fourth-, S_4, and sixth- (S_6) anisotropy parameters indicate changes in distribution sharpness, heterogeneity, and tail structure that cannot be inferred from Hermans anisotropy alone. Comparison with a generalized Maier-Saupe-type orientational distribution further suggests that surface modification promotes alignment pathways that deviate from unimodal nematic-like ordering, likely reflecting frustrated or heterogeneous nanoscale organization.

CRediT authorship contribution statement

Ases Akas Mishra: Writing – review & editing, Writing – original draft, Visualization, Methodology, Formal analysis, Data curation, Conceptualization; **Amit Kumar Sonker:** Writing – original draft, Methodology, Investigation, Conceptualization; **Kesavan Sekar:** Writing – review & editing, Visualization, Formal analysis, Data curation; **Marko Bek:** Writing – review & editing, Software, Formal analysis, Data curation; **Ann E. Terry:** Resources, Project administration, Methodology, Investigation, Funding acquisition, Formal analysis, Data curation, Conceptualization; **Kim Nygård:** Writing – review & editing, Resources, Project administration, Methodology, Investigation, Formal analysis, Conceptualization; **Stuart Ansell:** Software, Formal analysis; **Gunnar Westman:** Writing – review & editing, Validation, Supervision, Resources, Project administration, Methodology, Funding acquisition, Conceptualization; **Roland Kádár:** Writing – review & editing, Writing – original draft, Visualization, Validation, Supervision, Software, Resources, Project administration, Methodology, Investigation, Funding acquisition, Formal analysis, Data curation, Conceptualization.

Declaration of competing interest

The authors declare that they have no known competing financial interests or personal relationships that could have appeared to influence the work reported in this paper.

Acknowledgments

The work was supported by Chalmers Foundation through the project Chalmers Center for Advanced Neutron and X-ray scattering techniques in cooperation with MAX IV. The authors acknowledge MAX IV Laboratory for time on the CoSAXS beamline under proposal 20200458. Research conducted at MAX IV, a Swedish national user facility, was supported by the Swedish Research council under contract 2018–07152, the Swedish Governmental Agency for Innovation Systems under contract 2018–04969, and Formas under contract 2019–02496. AAM and RK are grateful to European Union's Horizon 2020 research and innovation programme under the Marie Skłodowska-Curie grant agreement No 955,605 YIELGAP and to Tetra Pak AB for their funding. AKS, KS, MB, GW and RK are grateful for the financial support of the Wallenberg Wood Science Centre (WWSC 3.0: KAW 2021.0313). RK acknowledges the additional financial support of the Chalmers Areas of Advance Materials, Nano and Production and that of the "2D material-based technology for industrial applications" 2D-TECH Vinnova Competence Centre (Ref. 2019-00068). The authors are grateful to Sylwia Wojno, Reza Ghanbari and Ehsan Hadi for supporting the SAXSb experiments, and to Prof. Christer Persson for proof-reading the manuscript.

Data availability

Data will be made available on request.

Supplementary material

Supplementary material associated with this article can be found in the online version at 10.1016/j.jcis.2026.140913.

Appendix A. Supplementary information

A.1. Anisotropy parameters

To generate a Legendre series, Rodrigues' formula can be used:

$$P_{2n}(x) = \frac{1}{2^{2n}2n!}\frac{d^{2n}}{dx^{2n}}\left[(x^2-1)^{2n}\right] \tag{A.1}$$

Based on this, the exact form of Hermans (2nd), 4th and 6th order anisotropy parameters within the integration limits used in this study are:

$$S_2 = \langle P_2(\cos\varphi)\rangle = \int_{-\pi/2}^{\pi/2} 0.5(3\cos^2\varphi - 1)w(\varphi)d\varphi \tag{A.2}$$

$$S_4 = \langle P_4(\cos\varphi)\rangle = \int_{-\pi/2}^{\pi/2} (1/8)(35\cos^4\varphi - 30\cos^2\varphi + 3)w(\varphi)d\varphi \tag{A.3}$$

$$S_6 = \langle P_6(\cos\varphi)\rangle = \int_{-\pi/2}^{\pi/2} \frac{1}{16}\left(231\cos^6\varphi - 315\cos^4\varphi + 105\cos^2\varphi - 5\right)w(\varphi) \tag{A.4}$$

A.2. Data processing and synchronization

All experimental data were processed using the *Multimodal Data Processor and Writer* (MuDPaW), version 5.8 [36]. MuDPaW is an open-source software framework developed within the Advanced Rheological Testing Science Initiative (artSI) at MAX IV. It is being specifically developed to support the analysis of rheological, optical, and scattering datasets acquired during multimodal experiments within artSI.

Version 5.8, see schematic below, includes thefollowing: connector for the CoSAXS and ForMAX beamlines at MAX IV; SAXS module; Rheo module; PLI module; PI module; Data writer (to template); and Batch data processor and writer. The connector is supporting automated normalization, background subtraction, and batch export of datasets. At present, a custom SSH connection must be installed manually. Core tasks such as file handling, metadata parsing, and synchronization logic are not detailed further here. In addition, The PI module is also an alpha-version while Tribo-SAXS is still being developed.

Data synchronization is performed with reference to the rheometry data, using three difference modalities: (a) triggered, where the SAXS data acquisition is triggered by the rheometer at interval steady state, (b) timed beamline data acquisition procedures, where SAXS data is acquired continuously and (c) using manual entries, where the duration of each interval, sleep times in-between and steady state window need to be inserted manually. For (a) and (b) modalities, a prescribed rheology data file is required to proceed. In this study, the experiments were not triggered, meaning the SAXS and rheology data were started simultaneously, however, steady state data needs to be extracted from the available transient rheology, SAXS and PLI data (modelity (b)). For each imposed shear-rate step, MuDPaW identifies the corresponding steady-state window and computes time-averaged quantities independently for each modality. If $x(t)$ denotes any time-resolved signal, the steady-state value is defined as

$$\overline{x}(\dot{\gamma}) = \frac{1}{\Delta t_{ss}}\int_{t_0}^{t_0+\Delta t_{ss}} x(t)\,\mathrm{d}t, \tag{A.5}$$

where t_0 and Δt_{ss} denote the start time and duration of the steady-state interval.

Overview of SAXS data processing. SAXS data processing within MuDPaW includes radial integration over the full accessible q-range and azimuthal integration over user-defined q-windows. Orientation parameters up to sixth order (S_2–S_6) can be computed via direct numerical integration or fitting-based approaches. Adaptive angular windowing and asymmetric peak integration are implemented to ensure robustness against beamstops and parasitic scattering. A two-peak analysis routine is available in beta form.

PLI processing. Polarized light imaging (PLI) data are processed by extracting intensity information along user-defined pixel paths from each video frame. Supported geometries include linear paths, circular arcs at arbitrary radii, and radial trajectories spanning the measurement gap. For each frame, RGB images are converted to the perceptually uniform CIELab color space [38].

Based on the extracted color-space components $L(\theta,t)$, $a(\theta,t)$, and $b(\theta,t)$, MuDPaW computes a range of scalar and distributed optical metrics, including the color-space norm

$$N(\theta,t) = \sqrt{L(\theta,t)^2 + a(\theta,t)^2 + b(\theta,t)^2}. \tag{A.6}$$

For a generic scalar quantity $y(\theta,t)$ derived from the optical data, path-resolved and integrated metrics can be computed. A commonly used measure is

$$A(\dot{\gamma}) = \int \langle y(\theta,t)\rangle_{t\in ss}\,\mathrm{d}\theta, \tag{A.7}$$

where $\langle\cdot\rangle_{t\in ss}$ denotes temporal averaging over the steady-state interval defined in Eq. A.5. Optional normalization relative to a reference condition may be applied.

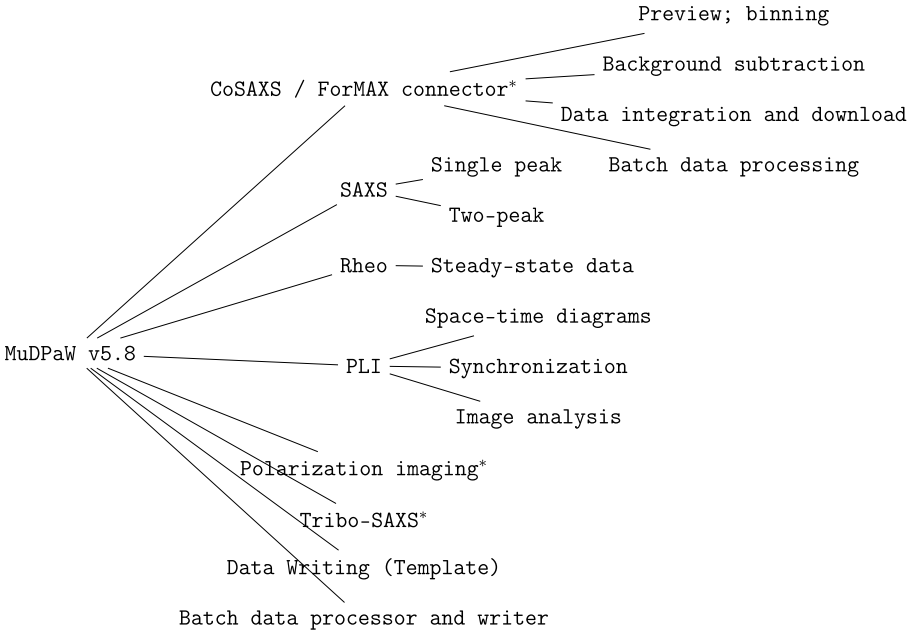

Additional features. A few powerful tools included in MuDPaW are not detailed here. They address specifically being able to make informed decisions even during beamtime measurements. Taken together, they represent the ability to extract large datasets from JypyterHub, bach-process them, and produce publication-ready graphs. The data in Fig. 3 is such an example. To enable this, we use as intermediate a proprietary external software, with the pipeline ready for artSI users. A current bottleneck is that rheological and PLI data need to be extracted from the respective computer devices and copied manually into the expected MuDPaW folder structure. In addition, PLI data takes longer to process than the rest of the data, depending on file size, and it has been a bit more difficult to batch process due to small adjustments that usually need to be made in the experimental setup during operation. Nevertheless, the batch processing pipeline has proven already to be essential for taking beamtime decisions based on preliminary data assessment and to speed up the coalescence of raw data into publication-grade graphs ready for interpretation. A new version, MuDPaW v6 is currently in the works with a much more seamless integration between the modules, and a more general formulation of the possible rheological tests, that should account for variable user adjustments sometimes inevitable during rheo-beamtimes.

A.3. Complementary data to Fig. 3

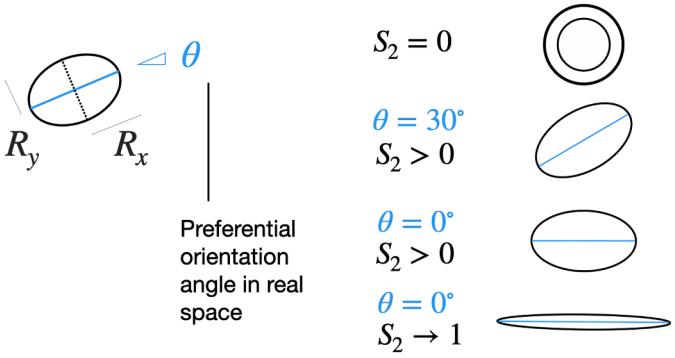

Fig. A.6. Illustration detailing the construction and significance of the SAXS datapoints in Fig. A.6: $R_x = S_{2,ref} + S_2(\dot{\gamma})$ and $R_y = S_{2,ref} - S_2(\dot{\gamma})$, where $S_{2,ref}$ is an arbitrary reference value. In all present experiments we have used $S_{2,ref} = 0.3$.

A.4. Maier–Saupe–type anisotropy distribution

In the classical Maier-Saupe mean-field theory for uniaxial nematic liquid crystals, the orientational distribution function (ODF) is given by [42]

$$f_{\mathrm{MS}}(\theta) \propto \exp\left[m\, P_2(\cos\theta)\right], \tag{A.8}$$

where θ denotes the polar angle of a particle orientation with respect to the director in real space, m is the Maier-Saupe interaction parameter, k_B is the Boltzmann constant, and T the temperature. Thus, parameter m can be used to control the width of the distribution: for $m = 0$ the distribution is isotropic, and increasing m corresponds to progressively stronger uniaxial alignment, see Fig. A.11a.

To allow for deviations from a purely unimodal Maier-Saupe distribution, we considered a lowest-order extension of this form, as expressed in Eq. (4). The equation introduces an additional shape parameter α_4. This extended form provides a minimal and controlled framework for exploring changes in the angular distribution beyond peak width alone, such as peak sharpening or shoulder formation. For $\alpha_4 = 0$, Eq. (4) reduces to Eq. (A.8).

It is important to emphasize that the experimentally accessible quantity in SAXS is not the three-dimensional ODF itself, but the azimuthal dependence of the scattered intensity, which represents a two-dimensional projection of the underlying orientational statistics. Consequently, the anisotropy parameters S_n extracted from the azimuthal intensity do not correspond directly to the moments of the true ODF, but rather to projected features of angular anisotropy. Nevertheless, reference trends generated from Eq. (4) provide a useful basis for comparing the interdependence of higher-order anisotropy parameters relative to S_2. Input distributions generated by varying m (and fixed α_4), together with the resulting anisotropy parameters and normalized higher-order anisotropy ratios, are presented in Fig. A.11.

We note that Eq. (4) is a truncated version of the general $f(\theta) \propto \exp\left(\sum_n \lambda_n P_n(\cos\theta)\right)$ which arises from the necessity of higher order tensors to determine alignment dynamics in liquid crystalline systems [45,46].

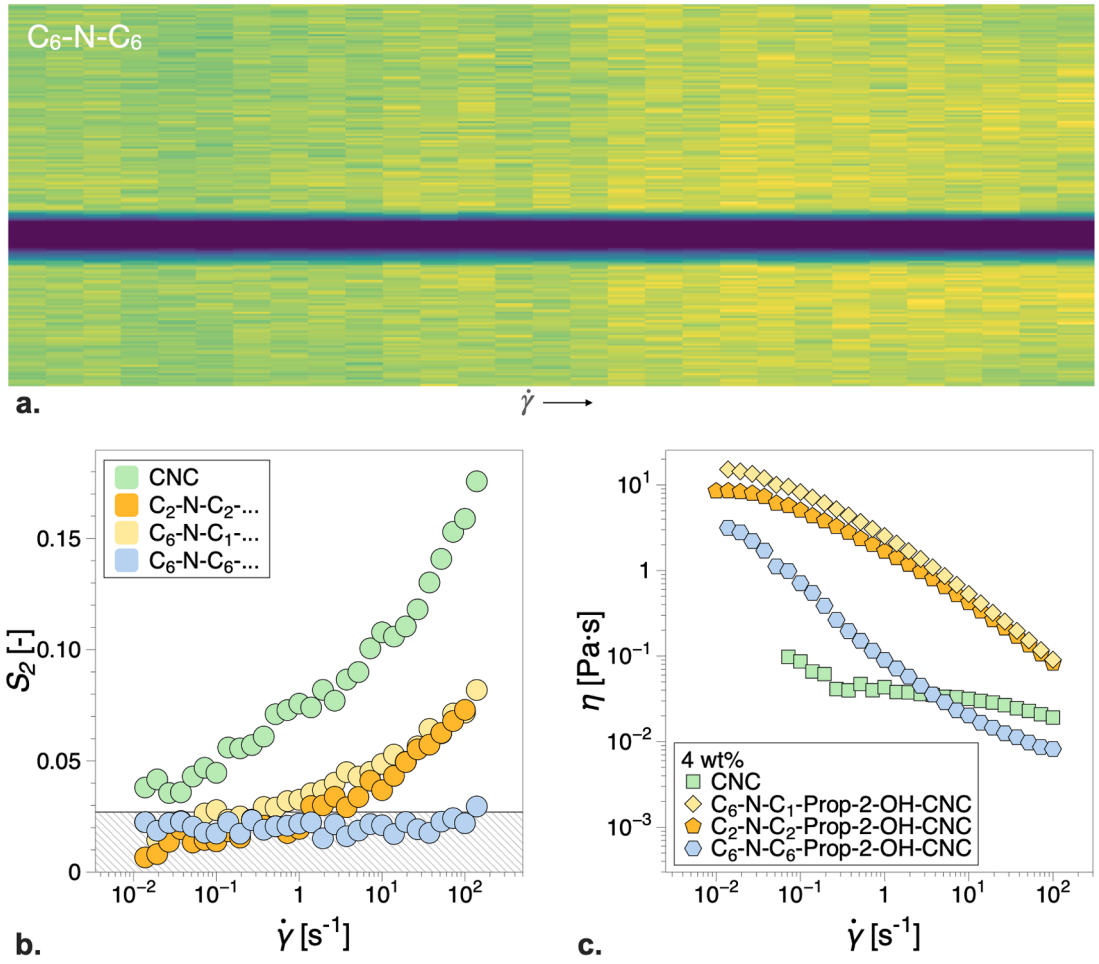

Fig. A.7. (a) Azimuthal integration data corresponding to C-$_6$-N-C$_6$ showing the absence of a reliably identifiable anisoptry peak. (b) Hermans anisotropy parameter, S_2, and (b) shear viscosity functions for the data in Fig. 3.

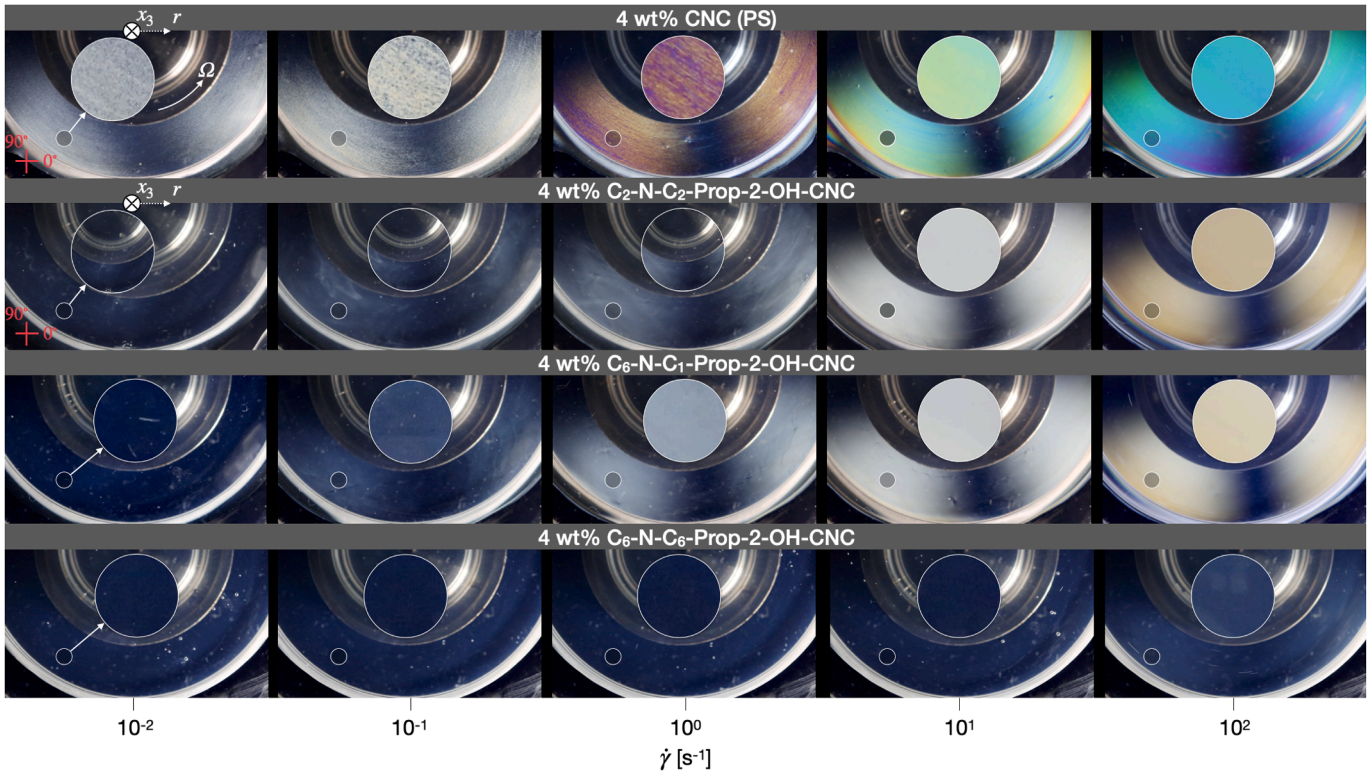

Fig. A.8. Still frames extracted from PLI videos showing the evolution of birefringence with shear rate for neat and surface modified CNC. samples.

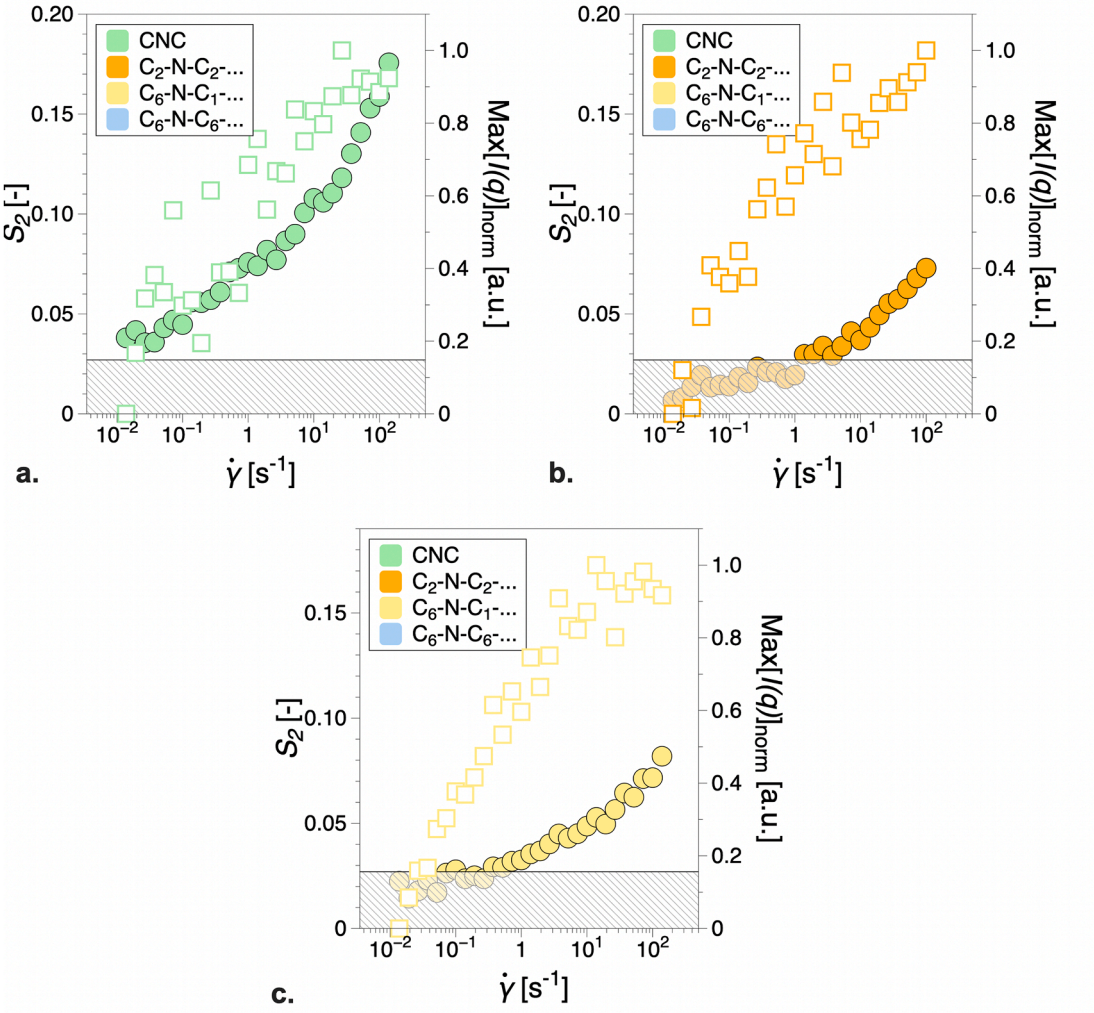

Fig. A.9. Comparison between the shear-rate dependence of S_2 and the normalised peak maxima in Fig. 4b, $I(q)_{\text{norm}} \in [0, 1]$.

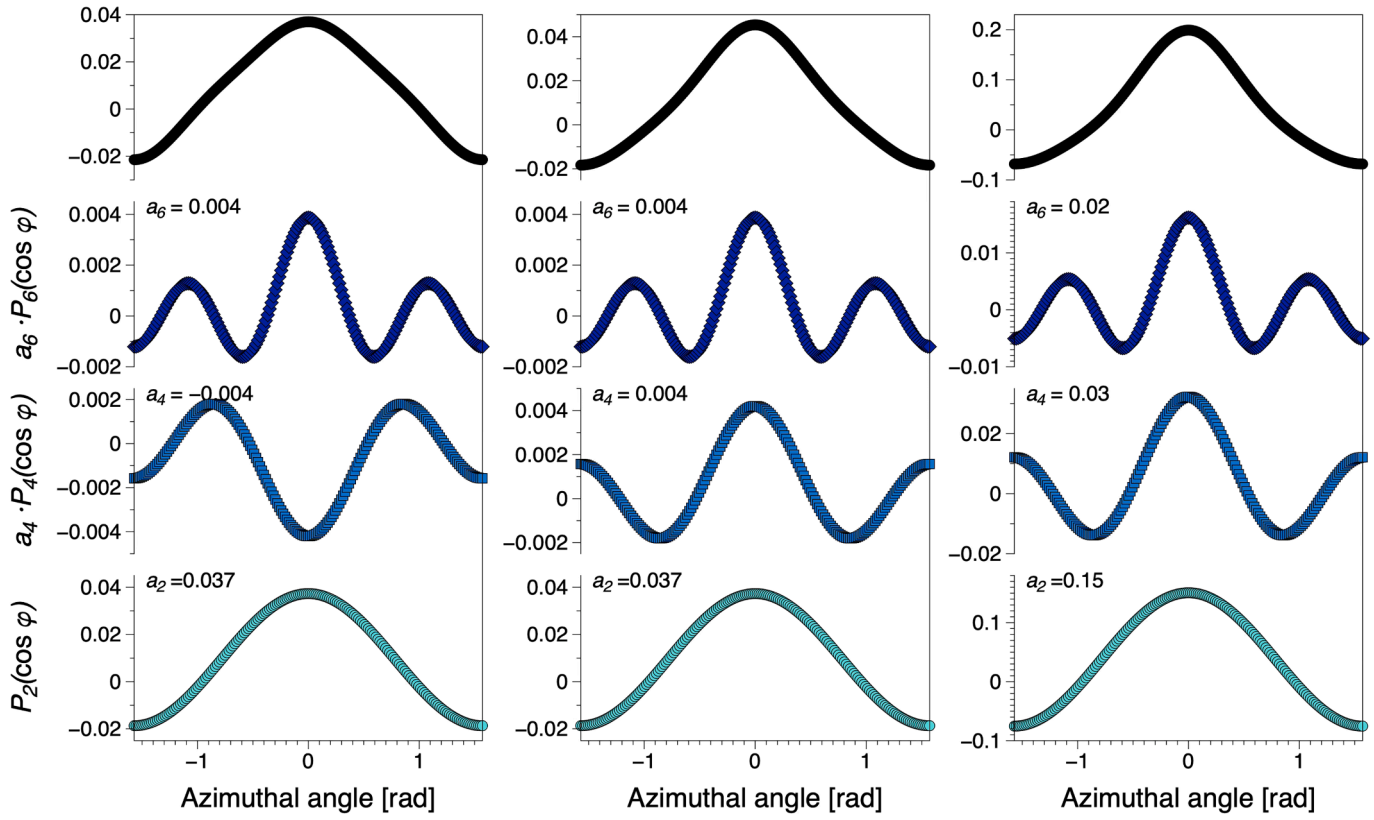

Fig. A.10. Illustration of the effect of higher-order Legendre terms on the angular shape of an orientation distribution, as $a_n \cdot P_2(\cos\varphi)$, $n = 2, 4, 6$, are shown together with their sum (top panels), for different combinations of coefficients.

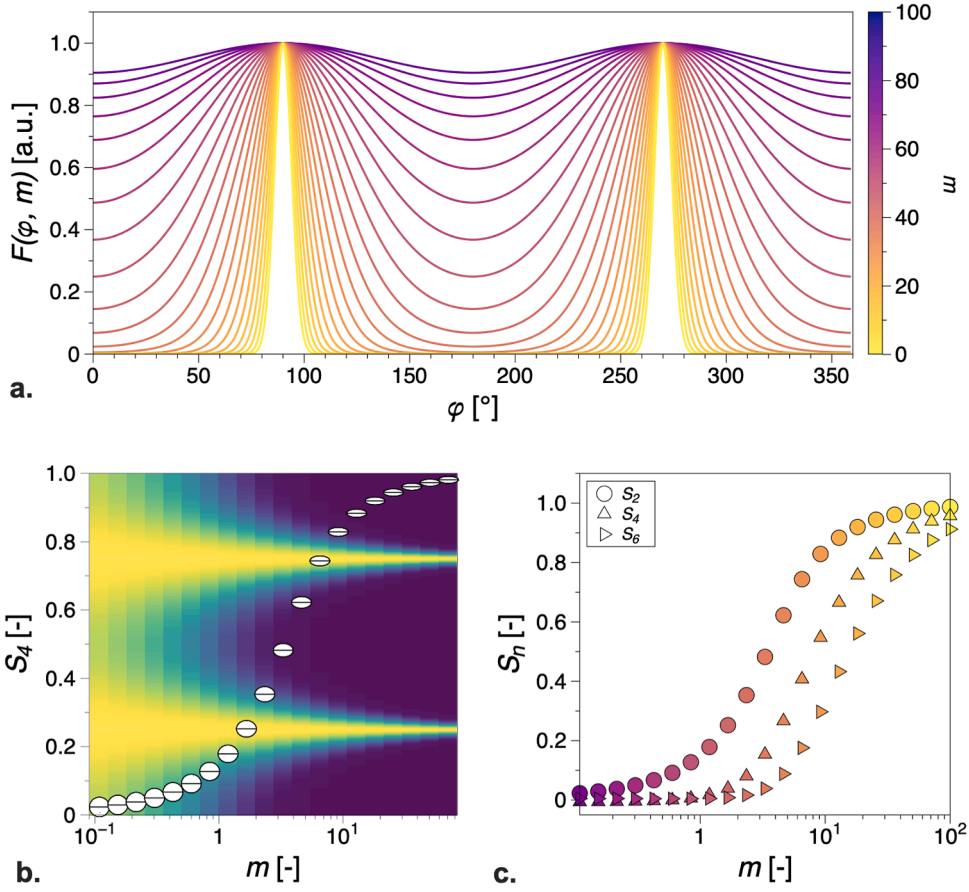

Fig. A.11. Anisotropy parameters based on the orientation distribution in Eq. (4) with $\alpha_4 = 0$: (a) azimuthal anisotropy distribution as function of m; note that $F(\varphi, m)$ is in this case considered to correspond to the scattering azimuthal intensity distribution $I(\varphi)$ in Eq. (2); (b) scalar intensity plot of the data in (a) with overlaid S_2 using the same representation as in Fig. 3; (c) comparison of $S_n(m)$, $n = 2, 4, 6$.

References

[1] T. Aziz Rohullah, A. Ullah, U. Zeb, M. Hussain, A. Ali, F. Haq, M. Kiran, Advancements in cellulose nanocrystals: a review of functionalization, applications, and challenges, Int. J. Biol. Macromol. 315 (2025) 144552.

[2] D. Trache, A.F. Tarchoun, M. Derradji, T.S. Hamidon, N. Masruchin, N. Brosse, M.H. Hussin, Nanocellulose: from fundamentals to advanced applications, Front. Chem. Volume 8 - 2020 (2020). https://doi.org/10.3389/fchem.2020.00392

[3] M. Ghasemlou, F. Daver, E.P. Ivanova, Y. Habibi, B. Adhikari, Surface modifications of nanocellulose: from synthesis to high-performance nanocomposites, Prog. Polym. Sci. 119 (2021) 101418.

[4] Y. Habibi, L.A. Lucia, O.J. Rojas, Cellulose nanocrystals: chemistry, self-Assembly, and applications, Chem. Rev. 110 (6) (2010) 3479–3500. https://doi.org/10.1021/cr900339w

[5] D. Klemm, F. Kramer, S. Moritz, T. Lindström, M. Ankerfors, D. Gray, A. Dorris, Nanocelluloses: a new family of nature-Based materials, Angew. Chem. Int. Ed. 50 (2011) 5438–66. https://doi.org/10.1002/anie.201001273

[6] R.J. Moon, A. Martini, J. Nairn, J. Simonsen, J. Youngblood, Cellulose nanomaterials review: structure, properties and nanocomposites, Chem. Soc. Rev. 40 (7) (2011) 3941–3994. https://doi.org/10.1039/C0CS00108B

[7] Z. Shi, S. Li, M. Li, L. Gan, J. Huang, Surface modification of cellulose nanocrystals towards new materials development, J. Appl. Polym. Sci. 138 (48) (2011) 51555.

[8] M. Börjesson, K. Sahlin, D. Bernin, G. Westman, Increased thermal stability of nanocellulose composites by functionalization of the sulfate groups on cellulose nanocrystals with azetidinium ions, J. Appl. Polym. Sci. 135 (10) (2018) 45963. https://doi.org/10.1002/app.45963

[9] L. Forsgren, K. Sahlin-Sjövold, A. Venkatesh, J. Thunberg, R. Kádár, A. Boldizar, G. Westman, M. Rigdahl, Composites with surface-grafted cellulose nanocrystals (CNC), J. Mater. Sci. 54 ((2019)) 3009-3022. https://doi.org/10.1007/s10853-018-3029-2

[10] M. Roman, W.T. Winter, Effect of sulfate groups from sulfuric acid hydrolysis on the thermal degradation behavior of bacterial cellulose, Biomacromolecules 5 (5) ((2004)) 1671–1677. https://doi.org/10.1021/bm034519+

[11] K. Sahlin, L. Forsgren, T. Moberg, D. Bernin, M. Rigdahl, G. Westman, Surface treatment of cellulose nanocrystals (CNC): effects on dispersion rheology, Cellulose 25 (1) (2018) 331–345. https://doi.org/10.1007/s10570-017-1582-5

[12] S. Wojno, A.K. Sonker, J. Feldhusen, G. Westman, R. Kádár, Isotropic gels of cellulose nanocrystals grafted with dialkyl groups: influence of surface group topology from nonlinear oscillatory shear, Langmuir 39 (18) (2023) 6433–6446.

[13] S. Wojno, A.K. Sonker, M. Garg, S. Cooper, M. Rigdahl, M. Linares, I. Zozoulenko, R. Kádár, G. Westman, Cellulose nanocrystal dispersions conjugated with symmetric and asymmetric dialkylamine groups, Cellulose 31 (11) (2024) 6705–6718.

[14] H. Tideland, J. Feldhusen, A.K. Sonker, G. Westman, Bendable transparent films from cellulose nanocrystals-study of surface and microstructure-property relationship, Carbohydr. Polym. Technol. Appl. 6 (2023) 100367. https://doi.org/10.1016/j.carpta.2023.100367

[15] A.K. Sonker, C. Kumar, H. Tideland, S. Bairagi, N.K. Katiyar, D.M. Mulvihill, G. Westman, Bendable substrates of cellulose nanocrystals for triboelectric nanogenerators, ACS Appl. Nano Mater. 8 (19) (2025) 9868–9877. https://doi.org/10.1021/acsanm.5c01087

[16] B.E. Droguet, H.-L. Liang, B. Frka-Petesic, R.M. Parker, M.F.L. De Volder, J.J. Baumberg, S. Vignolini, Large-scale fabrication of structurally coloured cellulose nanocrystal films and effect pigments, Nat. Mater. 21 (3) (2022) 352–358.

[17] M. Kröger, J. Vermant, The structure and rheology of complex fluids, 2000.

[18] T.G. Parton, R.M. Parker, G.T. van de Kerkhof, A. Narkevicius, J.S. Haataja, B. Frka-Petesic, S. Vignolini, Chiral self-assembly of cellulose nanocrystals is driven by crystallite bundles, Nat. Commun. 13 (1) (2022) 2657.

[19] J.-F. Revol, H. Bradford, J. Giasson, R.H. Marchessault, D.G. Gray, Helicoidal self-ordering of cellulose microfibrils in aqueous suspension, Int. J. Biol. Macromol. 14 (3) (1992) 170–172.

[20] L. Metilli, S. Mandin, I. Chazapi, E. Paineau, W. Chèvremont, N. Hengl, F. Pignon, B. Jean, Multi-scale investigation of the effect of photocurable polyethylene glycol diacrylate (PEGDA) on the self-assembly of cellulose nanocrystals (CNCs), J. Colloid Interface Sci. 685 (2025) 476–486.

[21] R. Kádár, S. Spirk, T. Nypelö, Cellulose nanocrystal liquid crystal phases: progress and challenges in characterization using rheology coupled to optics, scattering, and spectroscopy, ACS Nano 15 (5) (2021) 7931-7945.

[22] S. Shafeiei-Sabet, W.Y. Hamad, S.G. Hatzikiriakos, Influence of degree of sulfation on the rheology of cellulose nanocrystal suspensions, Rheol. Acta 52 (8–9) (2013) 741–751. https://doi.org/10.1007/s00397-013-0722-6

[23] S. Wojno, A. Ahlinder, A. Altskär, M. Stading, T. Abitbol, R. Kádár, Percolation and phase behavior in cellulose nanocrystal suspensions from nonlinear

rheological analysis, Carbohydr. Polym. 308 (2023) 120622. https://doi.org/10.1016/j.carbpol.2023.120622
[24] K. Nakamine, Y. Yokoyama, W.K.A. Worby, M. Muto, Y. Tagawa, Flow birefringence of cellulose nanocrystal suspensions in three-dimensional flow fields: revisiting the stress-optic law, Cellulose 31 (12) (2024) 7405–7420.
[25] B. Derakhshandeh, G. Petekidis, S. Shafiei Sabet, W.Y. Hamad, S.G. Hatzikiriakos, Ageing, yielding, and rheology of nanocrystalline cellulose suspensions, J. Rheol. 57 (1) (2013) 131–148.
[26] R. Kádár, M. Fazilati, T. Nypelö, Unexpected microphase transitions in flow towards nematic order of cellulose nanocrystals, Cellulose 27 (4) (2020) 2003–2014. https://doi.org/10.1007/s10570-019-02888-x
[27] M.K. Hausmann, P.A. Rühs, G. Siqueira, J. Läuger, R. Libanori, T. Zimmermann, A.R. Studart, Dynamics of cellulose nanocrystal alignment during 3D printing, ACS Nano 12 (7) (2018) 6926–6937.
[28] M. Araida, Y. Yamagata, S. Otobe, Y. Osafune, T. Sato, T. Katashima, G.H. McKinley, Analysis of the flow behavior of mechanically fibrillated cellulose nanofibril suspension by the rheo-Polarized imaging technique (rheo-Iris), Langmuir 41 (43) (2025) 29434–29445.
[29] F. Pignon, M. Challamel, A. De Geyer, M. Elchamaa, E.F. Semeraro, N. Hengl, B. Jean, J.-L. Putaux, E. Gicquel, J. Bras, S. Prevost, M. Sztucki, T. Narayanan, H. Djeridi, Breakdown and buildup mechanisms of cellulose nanocrystal suspensions under shear and upon relaxation probed by SAXS and SALS, Carbohydr. Polym. 260 (-) (2021) 117751.
[30] A.D. Haywood, K.M. Weigandt, P. Saha, M. Noor, M.J. Green, V.A. Davis, New insights into the flow and microstructural relaxation behavior of biphasic cellulose nanocrystal dispersions from rheoSANS, Soft Matter 13 (45) (2017) 8451–8462. https://doi.org/10.1039/C7SM00685C
[31] R. Ghanbari, A. Terry, S. Wojno, M. Bek, K. Sekar, A.K. Sonker, K. Nygård, V. Ghai, S. Bianco, M. Liebi, et al., Propagation of orientation across lengthscales in sheared self-Assembling hierarchical suspensions via rheo-PLI-SAXS, Adv. Sci. 12 (7) (2025) 2410920.
[32] O.O. Mykhaylyk, Time-resolved polarized light imaging of sheared materials: application to polymer crystallization, Soft Matter 6 (18) (2010) 4430–4440.
[33] L. Völker-Pop, Optical methods in rheology: polarized light imaging, Chem. Listy 108 (-) (2014) 697–724.
[34] S. Bianco, F. Hallam Stewart, S. Panja, A. Zyar, E. Bowley, M. Bek, R. Kádár, A. Terry, R. Appio, T.S. Plivelic, M. Maguire, H. Poptani, M. Marcello, R.R. Sonani, E.H. Egelman, D.J. Adams, Forging out-of-Equilibrium supramolecular gels, Nat. Synth. 3 (12) (2024) 1481–1489. https://doi.org/10.1038/s44160-024-00623-4
[35] M. Kahnt, K. Klementiev, V. Haghighat, C. Weninger, T.S. Plivelic, A.E. Terry, A. Björling, Measurement of the coherent beam properties at the coSAXS beamline, J. Synchrotron Radiat. 28 (6) (2021) 1948–1953.
[36] R. Kádár, M. Bek, MuDRaW: A Multimodal Data Processor and Writer, 2025. https://github.com/Rheology-and-Processing-of-Soft-Matter/RPSM_MuDRaW_v5.
[37] C.-P. Lafrance, A. Nabet, R.E. Prud'homme, M. Pézolet, On the relationship between the order parameter and the shape of orientation distributions, Can. J. Chem. 73 (1995) 1497–1505.
[38] Commission Internationale de l'Éclairage, Colorimetry, number 15 in CIE Publication, CIE Central Bureau, Vienna, Vienna, 1976.
[39] W. Maier, A. Saupe, Eine einfache molekulare theorie des nematischen kristallinflüssigen zustandes, Z. Für Naturforsch. a 13 (1958) 564–566. https://doi.org/10.1515/zna-1958-0716
[40] W. Maier, A. Saupe, Eine einfache molekular-statistische theorie der nematischen kristallinflüssigen phase. teil I, Zeitschrift für Naturforschung A 14 (1959) 882–889. https://doi.org/10.1515/zna-1959-1004
[41] W. Maier, A. Saupe, Eine einfache molekular-statistische theorie der nematischen kristallinflüssigen phase. teil II, Z. Für Naturforsch. a 15 (1960) 287–292. https://doi.org/10.1515/zna-1960-0409
[42] P.-G. de Gennes, J. Prost, The Physics of Liquid Crystals, Oxford University Press, Oxford, 2 edition, Oxford, 1993.
[43] J. Rooks, P.H. Gilbert, L. Porcar, Y. Liu, P. Butler, Anisotropy factors in small-angle scattering for dilute rigid-rod suspensions, J. Appl. Crystallogr. 56 (2023) 1–14. https://doi.org/10.1107/S1600576723002182
[44] T. Dabat, F. Hubert, E. Paineau, P. Launois, C. Laforest, B. Grégoire, B. Dazas, E. Tertre, A. Delville, E. Ferrage, A general orientation distribution function for clay-rich media, Nat. Commun. 10 (2019) 5456. https://doi.org/10.1038/s41467-019-13401-0
[45] S. Hess, Fokker–Planck-Equation approach to flow alignment in liquid crystals, Z. Für Naturforsch. a 31 (1976) 1034–1037. https://doi.org/10.1515/zna-1976-0820
[46] A.M. Sonnet, E.G. Virga, G.E. Durand, Dielectric shape dispersion and biaxial transitions in nematic liquid crystals, Phys. Rev. E 67 (6) (2003) 061701. https://doi.org/10.1103/PhysRevE.67.061701